J. Fluid Mech. (2021), *vol*. 915, A3, doi:10.1017/jfm.2020.1184

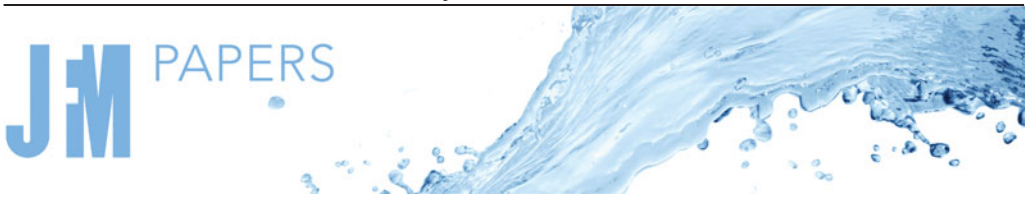

The impact of chemical modelling on turbulent premixed flame acoustics

D. Brouzet[1],†, M. Talei[1], M.J. Brear[1] and B. Cuenot[2]

[1]Department of Mechanical Engineering, University of Melbourne, Parkville, VIC 3010, Australia

[2]CERFACS, 42 Avenue Gaspard Coriolis, Toulouse Cedex 1 31057, France

(Received 28 June 2020; revised 8 November 2020; accepted 27 December 2020)

Direct numerical simulations are used to study the impact of chemical modelling on the flame dynamics and the sound generated by three-dimensional, turbulent, premixed methane/air jet flames. The semi-global BFER mechanism from Franzelli *et al.* (*Combust. Flame*, vol. 159, issue 2, 2012, pp. 621–637) and the more complex skeletal COFFEE mechanism from Coffee (*Combust. Flame*, vol. 55, issue 2, 1984, pp. 161–170) are considered. A more wrinkled flame is observed at downstream locations when using the COFFEE mechanism, demonstrating stronger flame/turbulence interaction. This flame also has a significantly lower acoustic power even though it features more acoustic output at high frequencies. The former is shown to arise from lower fluctuations of the heat release rate, whilst the latter is caused by the COFFEE mechanism creating more wrinkled flame surfaces. These results suggest that the accurate simulation of the noise emitted by turbulent premixed flames requires a chemical mechanism that ensures two main features: the heat release rate profile is important for modelling the overall sound amplitude and low frequency acoustics, whilst the flame/turbulence interaction impacts the higher frequency sound.

Key words: turbulent reacting flows, aeroacoustics

1. Introduction

In order to meet increasingly stringent emission standards, industrial gas turbines need to become more efficient and produce lower emissions. Operating these gas turbines with lean premixed flames can significantly contribute to this goal mainly by decreasing the combustion temperature, and therefore reducing the emissions of nitrogen oxides (Correa 1998; Wilfert *et al.* 2007). However, one challenge with combustors operating under lean conditions is thermo-acoustic instability. These instabilities arise from a resonant coupling between the unsteady flow, the combustion process and the combustor acoustics, resulting

† Email address for correspondence: davy.brouzet@gmail.com

in an unstable behaviour that is characterised by large, self-sustaining pressure oscillations. At best, gas turbines operating in an unstable regime require downtime for inspections and repair, whereas in extreme cases the instability can lead to gas turbine failure. Predicting and ultimately avoiding thermo-acoustic instability is therefore essential to the safe and efficient operation of gas turbines.

It has been shown that the sound generated by the combustion process, which is often termed as direct combustion noise, plays an important role in the triggering and dynamics of thermo-acoustic instability (Burnley & Culick 2000; Dowling & Mahmoudi 2015; Zhang *et al.* 2015; Poinsot 2017). Another type of noise generated in a gas turbine, called indirect combustion noise, occurs when the combustion products with non-uniform entropy, vorticity or mixture composition are accelerated through the outlet nozzle of the combustion chamber (Magri, O'Brien & Ihme 2016; Ihme 2017; Magri 2017). Even though indirect noise can be a significant contributor to the overall noise (Leyko, Nicoud & Poinsot 2009), the focus of this paper is on direct combustion noise.

Research on direct combustion noise goes back many decades, with one of the earliest studies undertaken by Thomas & Williams (1966). They studied sound generation by outwardly propagating laminar flames by igniting a soap bubble filled with a mixture of fuel and air. They revealed that the generated pressure waves were of monopolar nature, an observation that was also later reported in experimental studies of open, turbulent, premixed flames (Hurle *et al.* 1968; Price, Hurle & Sugden 1969; Abugov & Obrezkov 1978). Further experimental studies showed that combustion noise is also broadband in nature (Ramohalli 1979; Kotake & Takamoto 1987; Rajaram & Lieuwen 2009).

The fluctuations of the heat release rate have been shown to be the strongest source of noise in several studies of open, turbulent, low Mach number, premixed and non-premixed flames (Chiu & Summerfield 1974; Strahle 1978; Candel 2002; Ihme 2017). By rearranging the governing equations of fluid motion and using an acoustic analogy framework, Dowling (1992) developed a wave equation with several source terms. One of these source terms was proportional to the rate of change of the heat release rate $\partial\dot{Q}/\partial t$. Solution of this wave equation over an unbounded, homogeneous region, considering this source term only in a compact volume V is

$$p'(r_s, t) = \frac{\gamma - 1}{4\pi r_s c_\infty^2} \int_V \frac{\partial \dot{Q}}{\partial t} (t - r_s/c_\infty)\, \mathrm{d}V, \tag{1.1}$$

where p' represents the fluctuations of pressure, r_s is the distance from the flame to the receiver, γ is the heat capacity ratio and c_∞ is the speed of sound in the propagation medium, far from the flame. Equation (1.1) was used in several studies to either compute the contribution of the heat release rate fluctuations to the overall sound (Ihme, Pitsch & Bodony 2009; Ihme & Pitsch 2012; Zhang *et al.* 2013; Brouzet *et al.* 2019) or to establish scaling laws (Rajaram, Gray & Lieuwen 2006; Haghiri *et al.* 2018).

Equation (1.1) also highlights that accurate calculation of combustion noise requires accurate representation of $\partial\dot{Q}/\partial t$. This, in turn, suggests that accurate modelling of the flame chemistry may also be important. While detailed chemical kinetic mechanisms for small hydrocarbon fuels are available (e.g. Smith *et al.* 1999; Metcalfe *et al.* 2013) their use results in significant computational costs, since they consider a large number of species and reactions. In order to make three-dimensional (3-D) simulations of reacting flows computationally affordable, such chemistry mechanisms therefore need to be reduced. This can be achieved by eliminating species and reactions absent from the main chemical pathways, to create a skeletal mechanism. In the limit where a mechanism is reduced to one overall reaction, the reduced scheme is referred to as global. An alternative is to keep

a few important reactions in a semi-global mechanism. To develop a reduced chemical mechanism, parameters such as the adiabatic flame temperature, the laminar flame speed and/or the ignition delay are usually used as metrics in the reduction process (Lovas *et al.* 2002; Zheng, Lu & Law 2007; Metcalfe *et al.* 2013). However, none of these quantities guarantees that $\partial\dot{Q}/\partial t$ can be correctly captured in a turbulent flame. As the number of removed species increases, the heat release rate profile will increasingly differ from that obtained with the original mechanism, potentially to the point where it significantly alters the resulting combustion noise. In this way, chemical modelling may directly affect the flame acoustics.

An alternative approach to the direct calculation of $\partial\dot{Q}/\partial t$ in (1.1) is to use flamelet theory and relate this term to the rate of change of the flame surface area $\mathrm{d}A/\mathrm{d}t$ (Abugov & Obrezkov 1978; Clavin & Siggia 1991), so that

$$\int_V \partial\dot{Q}/\partial t \,\mathrm{d}V = c_p(T_b - T_u)\rho_u S_L \,\mathrm{d}A/\mathrm{d}t. \tag{1.2}$$

In this formulation, c_p is the heat capacity at constant pressure, T and ρ are the temperature and density of the medium, respectively, S_L is the laminar flame speed, and the subscripts u and b refer to the values in the unburnt and burnt mixture, respectively. Assuming a thin flame front, the far field sound can be obtained (Candel *et al.* 2009),

$$p'(r_s, t) = \frac{\rho_\infty}{4\pi r_s}\left(\frac{\rho_u}{\rho_b} - 1\right) S_L \left[\frac{\mathrm{d}A}{\mathrm{d}t}\right]_{t-r_s/c_\infty}. \tag{1.3}$$

It is important to note that (1.2) and (1.3) are valid only when the consumption speed S_c is constant and equal to S_L. If the fuel Lewis number Le is unity, asymptotic studies found that S_c is insensitive to strain for small stretch values (Matalon & Matkowsky 1982; Pelce & Clavin 1982; Clavin 1985; Klimenko & Class 2000). Equation (1.3) has been used to compute the sound radiated by perturbed laminar flames (Schuller, Durox & Candel 2002) and turbulent flames (Belliard 1997; Truffaut 1998), highlighting the importance of flame dynamics in the sound generation process. Chemical modelling can therefore play a role through global flame parameters such as S_L, and also via its impact on the evolution of the flame surface area.

Many numerical studies have examined the effects of chemical modelling on premixed flames, as reviewed by Hilbert *et al.* (2004). Hilka *et al.* (1995) simulated a vortex pair interacting with a lean methane/air premixed flame with a skeletal and a semi-global mechanism. Significant discrepancies were observed in the heat release and local production rates, mainly due to strain and curvature effects. In their study of hydrogen/air premixed flames, Baum *et al.* (1994) noted that flames modelled using detailed chemistry are more sensitive to strain compared with their counterparts which use a global mechanism. Franzelli (2011) noted that the use of semi-global mechanisms in a homogeneous, isotropic turbulent field could lead to an under-estimation of the flame thickness and an over-estimation of the flame surface area.

It is worth noting that only a few studies have analysed the effect of chemical modelling on sound generation by premixed flames. Jimenez *et al.* (2015) compared sound generation by one-dimensional (1-D) hydrogen/air premixed flame annihilation using global and detailed mechanisms. They found that simple chemistry can be sufficient for predicting the generated sound amplitude when the Lewis number is less than or equal to unity. Ghani & Poinsot (2017) investigated sound generation by a 1-D head-on-quenching of a methane-air premixed flame. In this configuration, semi-global chemistry can lead to an over-estimation of the pressure amplitude for stoichiometric flames. This difference

was related to the semi-global mechanism's higher reaction rate in the post-flame region after the flame quenched. Another study on 1-D annihilation events (Brouzet *et al.* 2018) confirmed the importance of slow reactions occurring in the post-flame region for sound generation. It should be noted that all of these studies were limited to 1-D laminar flames and the conclusions might be different for 3-D turbulent flames.

The aim of this paper is therefore to address this gap by examining the impact of chemical modelling on turbulent premixed jet flame acoustics. Direct numerical simulations (DNS) of 3-D turbulent premixed jet flames with high-fidelity acoustics are performed, using a semi-global and skeletal methane/air chemistry mechanism. The theoretical framework developed to relate chemical modelling and flame dynamics to combustion noise is first presented. The DNS results are then analysed by assessing the impact of chemical modelling on the flame dynamics and flame/turbulence interaction. Combustion noise is then examined by first considering the heat release rate fluctuations as the primary source of noise, and then relating the flame dynamics to the far field noise.

2. Direct numerical simulation dataset

2.1. *Numerical methods*

The DNS carried out in this study were performed using the code NTMIX-CHEMKIN, an accurate high-order solver designed to perform simulations of reacting flows with reduced and detailed chemical kinetic models (Baum *et al.* 1994). This code has been frequently used in DNS studies of reacting flows (Haworth *et al.* 2000; Jimenez *et al.* 2002; Jimenez & Kurdyumov 2017; Jiang, Gordon & Talei 2019; Palulli, Talei & Gordon 2019; Rivera *et al.* 2019). The code solves the fully compressible Navier–Stokes, energy and species conservation equations in a Cartesian coordinates system $[x, y, z]$, where x, y and z denote the streamiwse, transverse and spanwise directions, respectively. The code uses an eight-order explicit central spatial differencing scheme and a low-storage third-order Runge–Kutta time integrator. The ideal gas law is used to relate pressure, density and temperature. Species production and molecular transport terms are obtained using the CHEMKIN and TRANSPORT packages (Kee, Rupley & Miller 1989). The diffusion velocities are modelled using mixture-based species-specific diffusivities (Baum, Poinsot & Thevenin 1995). The Dufour effect is established by neglecting the effects of pressure gradients. Additionally, the Soret effect on the species diffusion velocities is accounted for. The full set of equations, and more details about the upcoming DNS description, can be found in the work of Brouzet (2019).

NTMIX-CHEMKIN uses a tenth-order explicit filter, with an appropriate boundary closure from Kennedy & Carpenter (1994), to artificially damp high frequency numerical waves. Tests on the DNS cases showed that applying this filter every 5 time steps with a damping amplitude equal to 0.2 was sufficient to remove the spurious waves.

The 1-D Navier–Stokes characteristic boundary condition for reacting flows from Baum *et al.* (1995) is used in the present work to treat the non-reflecting subsonic outflow boundaries and relaxing the pressure to the ambient mean pressure. The relaxation constant was chosen following the optimum value proposed by Rudy & Strikwerda (1980).

To impose the turbulent velocity fluctuations at the jet inlet, a frozen spatial 3-D isotropic turbulent field following the Passot–Pouquet spectrum (Passot & Pouquet 1987) was first generated. The frozen isotropic turbulent field was then rescaled using the turbulence intensity profiles of Wu & Moin (2008). The generated velocity fluctuations were then added to the mean streamwise velocity pipe flow profile. The resulting turbulent field was injected into the domain at a convective speed of $U_{conv} = 0.75\bar{u}_c$, using Taylor's

Mechanism	Species	Reactions	T_b^* [K]	S_L^* [cm s^{-1}]
BFER	6	2	2480	180.4
COFFEE	14	38	2422	184.7
GRI 3.0	53	325	2419	173.4

Table 1. Characteristics of the two chemical mechanisms considered in this work (Coffee 1984; Franzelli *et al.* 2012) compared with GRI3.0 (Smith *et al.* 1999). The burnt gas temperature (T_b^*) and laminar flame speed (S_L^*) are for a stoichiometric laminar flame with an unburnt gas temperature of $T_u^* = 700$ K.

hypothesis, where $\bar{u}_c$ is the mean centreline inlet velocity. The chosen convective velocity lies in the range recommended by Choi & Moin (1990) for the injection of wall-bounded turbulence and is in agreement with several experimental studies on the applicability of Taylor's hypothesis in turbulent round jets (Wills 1964; Ko & Davies 1971; Moore 1977).

2.2. *Chemical mechanisms*

Two methane/air chemical mechanisms were used in the DNS conducted in this work. The goal is to compare a heavily reduced mechanism which is of interest to the computational fluid dynamics community and a more detailed one which keeps the main chemical pathways while being computationally affordable for a 3-D DNS. We therefore chose a semi-global and a skeletal mechanism, which are presented below and are summarised in table 1. The complete set of reactions and chemistry constants can be found in appendix A.

The semi-global two-steps BFER mechanism for methane/air mixtures (Franzelli *et al.* 2012) features sixspecies, namely CH_4, O_2, H_2O, CO_2, CO and N_2. It has been validated for a range of unburnt gas temperatures (300 to 700 K), pressures (1 to 15 atm) and equivalence ratios ($\phi = 0.6$ to 1.4) by comparing the laminar flame speed and adiabatic flame temperature to those obtained from GRI3.0 (Smith *et al.* 1999). This very affordable mechanism has been used in numerous large eddy simulations of fluidised bed reactors (Dufresnes *et al.* 2016) and swirled burners (Franzelli *et al.* 2012; Cuenot, Riber & Franzelli 2014; Cheneau, Vie & Ducruix 2015; Lourier *et al.* 2017).

The skeletal COFFEE mechanism (Coffee 1984) features 38 reactions and 14 species. It has been validated with experimental data of premixed methane/air flames at 300 K and atmospheric pressure. Species and temperature profiles, as well as the laminar flame speed, were in good agreement with experimental results for equivalence ratios ranging from 0.85 to 1.25.

The BFER and COFFEE mechanisms were used to perform a DNS of a turbulent premixed flame under stoichiometric conditions ($\phi = 1$) at the unburnt gas temperature $T_u^* = 700$ K, typical of gas turbine compressor exit temperatures. Here and in the following, the superscript * refers to dimensional quantities. The adiabatic flame temperature and the laminar flame speed at the same ϕ and T_u^* using the BFER and COFFEE mechanisms are compared with the results obtained with the detailed GRI3.0 mechanism in table 1. The two reduced mechanisms show a good agreement with the detailed chemistry mechanism for these quantities, as the largest error equals 6.5 % for the laminar flame speed obtained with the COFFEE mechanism. As shown by Brouzet *et al.* (2018), there is also a good agreement between GRI 3.0 and COFFEE when sound generation by 1-D flame annihilation is examined. In addition, a good agreement between COFFEE and GRI3.0 was observed for the thermal flame thickness and the heat release rate profile at the conditions used in this study. For readability, the datasets performed with

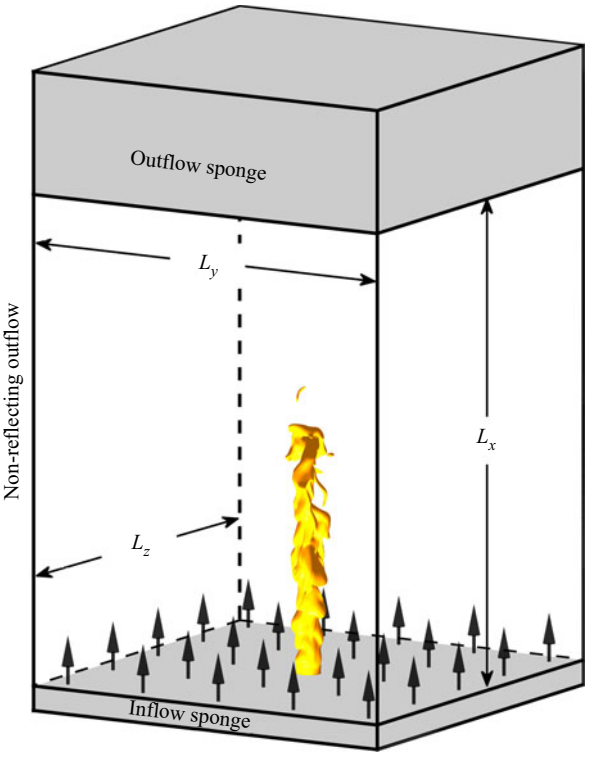

Figure 1. Schematic of the DNS configuration. The grey areas represent the sponge layers (see § 2.4) and the arrows represent the coflow.

the semi-global BFER and skeletal COFFEE chemical mechanisms are referred to simply as the BFER and COFFEE cases, respectively.

2.3. *Direct numerical simulation configuration and set-up*

The cases considered feature a turbulent, premixed, methane/air, round-jet flame in an open environment of combustion products at the adiabatic flame temperature and at atmospheric pressure. The inlet jet Reynolds number Re is equal to 5300 and the Mach number M is 0.36. A coflow with 1 % of the mean inlet Mach number surrounds the jet to ensure the stability of the flame. The temperature and mass fractions are imposed at the inlet using an unstrained, freely propagating laminar flame solution (Sankaran *et al.* 2007) so that the maximum temperature gradient in the radial direction is located at $r/D = 0.5$ (where D is the inlet jet diameter). A schematic representation of the computational domain is shown in figure 1.

The Karlovitz number is above unity for the cases considered and the Kolmogorov length scale is slightly smaller than the diffusive flame thickness $\delta_f \sim \nu/S_L$ (see table 2), where ν represents the kinematic viscosity. This means that the turbulent flames are in the 'thin reaction zone' regime. All relevant flow and flame parameters are shown in table 2, in dimensionless form. The reference values used for non-dimensionalising the quantities presented throughout the paper are shown in table 3.

An extensive grid independence study showed that 10 points per thermal flame thickness (pts/δ_{th}) in the streamwise direction and 12 pts/δ_{th} in the transverse/spanwise directions

Parameters	BFER	COFFEE
Physical domain size ($L_x \times L_y \times L_z$)	$20D \times 16D \times 16D$	
Grid size ($N_x \times N_y \times N_z$)	$1811 \times 721 \times 721$	$1546 \times 676 \times 676$
Minimum grid spacing ($\Delta x/\delta_{th}$) in the streamwise direction	10	12
Minimum grid spacing ($\Delta x/\delta_{th}$) in the transverse and spanwise directions	12	16
Equivalence ratio (ϕ)	1	1
Ratio of burnt to unburnt gas temperature (T_b/T_u)	3.54	3.46
Mean inlet Mach number ($M = \bar{u}_{in}/c_{in}$)	0.36	0.36
Inlet bulk velocity (U_{bulk})	0.27	0.27
Jet Reynolds number ($Re = \bar{u}_{in}D/\nu$)	5300	5300
Inlet streamwise turbulence intensity ($u_p = u_{x,rms}/c_{in}$) at centreline	0.0133	0.0133
Integral longitudinal length scale (l_t/D)	0.30	0.30
Turbulent Reynolds number ($Re_t = u_p l_t/\nu$)	58.8	58.8
Laminar flame speed (S_L)	3.41×10^{-3}	3.49×10^{-3}
Thermal flame thickness (δ_{th}/D)	0.1	0.158
Diffusive flame thickness (δ_f/D)	0.02	0.02
Ratio of turbulence intensity to laminar flame speed (u_p/S_L)	3.90	3.81
Size of most energetic eddies (λ_e/D)	0.75	0.75
Kolmogorov length scale (η/D)	0.014	0.014
Karlovitz number ($Ka = \delta_{th}\nu/(S_L\eta^2)$)	9.98	15.43
Damkohler number ($Da = l_t S_L/(u_p\delta_{th})$)	0.77	0.50
Average flame length (L_{flame}/D)	14	12.9
Flow through time ($\tau_f = L_x/\bar{u}_{in}$)	56	56

Table 2. Flow and flame parameters for the DNS. All quantities are dimensionless and the *in* subscript denotes the values at the inlet.

Quantity	Expression	Value
Length	$L_{ref} = D$	1.85×10^{-1} cm
Velocity	c_{ref}	5.29×10^{4} cm s^{-1}
Density	ρ_{ref}	4.81×10^{-4} g cm^{-3}
Heat capacity	$c_{p,ref}$	1.22×10^{7} cm^2 s^{-2} K^{-1}
Time	$t_{ref} = L_{ref}/c_{ref}$	3.50×10^{-6} s
Frequency	$f_{ref} = c_{ref}/L_{ref}$	2.85×10^{5} s^{-1}
Temperature	$T_{ref} = c_{ref}^2/c_{p,ref}$	2.29×10^{2} K
Pressure	$p_{ref} = \rho_{ref}c_{ref}^2$	1.35×10^{6} g cm^{-1} s^{-2}
Energy	$e_{t,ref} = c_{ref}^2$	2.80×10^{9} cm^2 s^{-2}
Heat release rate	$\dot{Q}_{ref} = \rho_{ref}c_{ref}^3/L_{ref}$	3.84×10^{11} g cm^{-1} s^{-3}

Table 3. Reference values used for non-dimensionalisation.

were necessary to suppress the numerical noise emitted by the flame, when using the BFER mechanism. For the COFFEE mechanism, 12 pts/δ_{th} in the streamwise direction and 16 pts/δ_{th} in the transverse/spanwise directions were necessary. In the streamwise

direction the grid spacing was kept constant up to the end of the physical domain. In the transverse/spanwise directions the grid was stretched for $|y|$, $|z| > 1.2D$ to reduce the number of grid points in the domain. As recommended by other acoustic studies, the grid stretching $\zeta = \Delta x_{i+1}/\Delta x_i - 1$ was below 2 % to avoid any potential spurious waves (Mitchell 1996; Haghiri *et al.* 2018).

Statistical convergence was verified by analysing the temporal mean and root mean square (r.m.s.) statistics of the volume integral of the heat release rate, the streamwise velocity at the farthest streamwise centreline location and the pressure fluctuations in the far field. All quantities converged after $5\tau_f$, where τ_f represents the flow through time $L_x/\bar{u}_{in}$, reaching statistically steady mean and r.m.s. values. The production runs were therefore commenced after $5\tau_f$, and were run for $3.5\tau_f$, long enough to capture the acoustic spectrum peak (see § 4.2). The computational costs for the BFER and COFFEE production runs were equal to 540 000 CPU-h and 640 000 CPU-h, respectively, running on 9216 Intel Xeon E5-2690V3 'Haswell' processors. This corresponds to a physical computational time of 58 and 70 h for the BFER and COFFEE cases, respectively.

2.4. *Sponge layers*

Two major acoustic-related issues needed to be addressed. Firstly, strong acoustic reflections from the outflow boundary were observed. Secondly, the turbulent velocity field imposed at the inflow led to a significant emission of sound, which was dominating the noise generated by the combustion process at some wavelengths. Since the focus of this study is on direct combustion noise, it was necessary to eliminate the outflow reflections and damp the inflow noise from the injected synthetic turbulence. To do so, sponge layers were used for both inflow and outflow boundaries.

In the sponge layers, the right-hand side of the governing equations were modified so that the solution for a quantity q is driven to a target solution $q_0(\boldsymbol{x}, t)$,

$$\frac{\partial q}{\partial t} = \cdots - \sigma(\boldsymbol{x})(q - q_0(\boldsymbol{x}, t)), \tag{2.1}$$

where $\sigma(\boldsymbol{x})$ is the relaxation function.

2.4.1. *Outflow boundary*

The sponge layer at the outflow spanned from $x_{min} = 20D$ to $x_{max} = 25D$. A quadratic relaxation function was used (Bogey, Bailly & Juve 2000),

$$\sigma(x) = \sigma_{max}\left(\frac{x - x_{min}}{x_{max} - x_{min}}\right)^2, \tag{2.2}$$

where the maximum relaxation value σ_{max} was chosen to damp the fluctuations in the sponge layer without altering the upstream field or introducing spurious reflections. Only the right-hand side of the momentum equations were altered, to damp the velocity fluctuations in the sponge layer close to the outflow boundary. The target value $q_0(\boldsymbol{x})$ was set to zero for the transverse and spanwise directions. In the streamwise direction the target velocity was obtained using the self-similar solution for round-jet flows from Hussein,

Capp & George (1994),

$$[\rho U]_0\,(x, r) = \rho B_0 \frac{(M_0)^{1/2}}{x} \exp\left[-A_0\left(\frac{r}{C_0 x}\right)^2\right], \tag{2.3}$$

where the constant A_0 has a value of 0.693. The two empirical factors $B_0 = 6.0$ (decaying coefficient) and $C_0 = 0.09$ (spreading coefficient) were obtained by fitting the function to the temporally averaged streamwise velocity field using least-squares regression. The variable M_0 in (2.3) represents the integral of the momentum flux per unit mass $\int u^2\,\mathrm{d}A$ at the jet inlet.

2.4.2. *Inflow boundary*

Equation (2.1) was proposed by Freund (1997) to prevent non-physical acoustic radiation from the inflow, when a turbulent flow was imposed at the inlet. Freund (1997) suggested that $q_0(\boldsymbol{x})$ could be computed by solving the governing equations using the convection terms only. In the present work, Taylor's hypothesis was used to compute the target solutions. The target values for the density, momentum, energy and species equations were then defined respectively as

$$[\rho]_0\,(x, t) = \rho_{in}, \tag{2.4}$$

$$[\rho \boldsymbol{u}]_0\,(x, t) = \rho_{in}\boldsymbol{u}_{in}(t - x/U_{conv}), \tag{2.5}$$

$$[\rho e_t]_0\,(x, t) = \tfrac{1}{2}\rho_{in}\boldsymbol{u}_{in}^2(t - x/U_{conv}) - p(x, t) + \sum_{\alpha=1}^{N_s} \rho_{in} h_{\alpha,in} Y_{\alpha,in} \quad \text{and} \tag{2.6}$$

$$[\rho Y_\alpha]_0\,(x, t) = \rho_{in} Y_{\alpha,in}, \tag{2.7}$$

where $\boldsymbol{u}$ is the gas velocity vector, e_t is the total energy, h is the enthalpy, Y is the mass fraction, N_s represents the number of species in the chemical mechanism considered and the subscript α denotes the quantities related to species α. The target values of momentum and kinetic energy in (2.5) and (2.6) are defined based on Taylor's hypothesis of a frozen turbulent field. The convective velocity U_{conv} was set to $0.75\bar{u}_c$, consistent with the convective speed used for the injection of turbulence. The inlet sponge layer spanned from $x_{min} = -1D$ to $x_{max} = 0$. Freund (1997) suggested a relaxation function that was of cubic form, forcing the first three derivatives of the function and the solution to be continuous across the sponge/physical domain interface. He also noted that a hyperbolic-tangent-based function, that becomes exponentially small within the sponge layer, can also be used. Preliminary tests showed that using either a cubic or a tangent hyperbolic function resulted in a radial expansion of the jet throughout the sponge layer, leading to velocity fluctuations at the end of the sponge layer that were not representative of a pipe flow. The relaxation function was therefore modified to limit the jet expansion. In the jet region ($r/D \leqslant 0.5$), the relaxation function followed a cubic decay whereas the function was tangent-hyperbolic-like in the coflow region ($r/D > 0.5$). As can be seen in figure 2, for a large portion of the sponge layer, the coflow region has a significantly larger relaxation value than that in the jet region, effectively restricting the jet expansion. The exact form of the relaxation function is

$$\sigma\,(x, r) = \sigma_{jet}(x) = \sigma_{max}(1 - x)^3 \quad \text{for } r/D \leqslant 0.5; \tag{2.8}$$

$$\sigma\,(x, r) = \sigma_{coflow}(x) = \frac{\sigma_{max}}{2}\left[1 + \tanh(C_{s,1} \cdot (C_{s,2} - x))\right] \quad \text{for } r/D > 0.5. \tag{2.9}$$

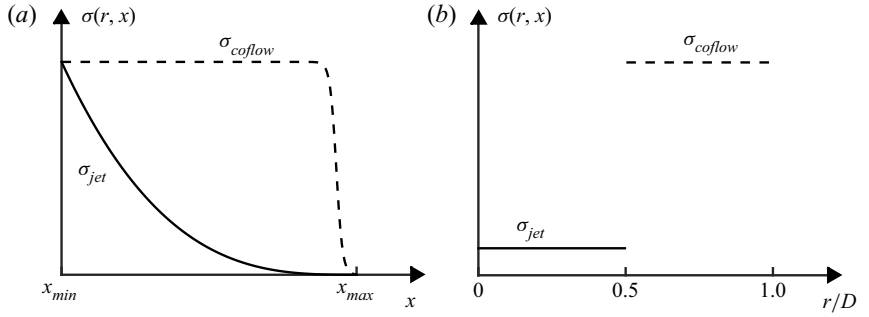

Figure 2. Representation of the relaxation function σ used for the inlet sponge layer in the streamwise (a) and radial (b) directions. The terms σ_{jet} (solid line) and σ_{coflow} (dashed line) denote the function in the jet region ($r/D \leqslant 0.5$) and in the coflow region ($r/D > 0.5$), respectively.

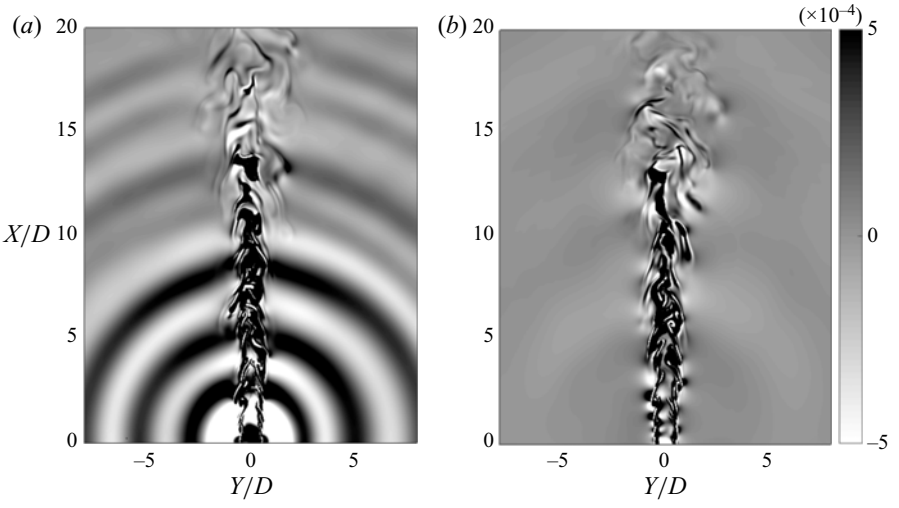

Figure 3. Dilatation field of the BFER case without the inlet sponge layer (a) and with the inlet sponge layer (b).

The parameter σ_{max} represents the maximum relaxation value, which was set to a value that led to minimal jet expansion while ensuring numerical stability. The constants $C_{s,1}$ and $C_{s,2}$ defined the shape of the tangent hyperbolic profile, and were chosen (1) to minimise acoustic reflections and (2) to ensure the relaxation function is infinitesimally small at the end of the sponge layer.

Figure 3 shows the dilatation field $\nabla \cdot \boldsymbol{u}$ of the BFER case, both with and without the inlet sponge. The dilatation represents the divergence of the flow velocity field, which has been shown to be directly related to the pressure in the far field through the following equation (Colonius, Lele & Moin 1997):

$$\frac{\partial p}{\partial t} + \rho_\infty c_\infty \nabla \cdot \boldsymbol{u} = 0, \tag{2.10}$$

Figure 3 shows that the inlet sponge has significantly reduced the noise generated from the injection of turbulence. In addition, the flow field statistics downstream of the inlet were not significantly affected by the presence of the sponge layer at the inlet.

3. Theoretical framework

3.1. *Relationship between heat release rate and combustion noise*

The heat release rate term appearing in the governing equation for the sensible enthalpy is used in the following (Poinsot & Veynante 2005, p. 18):

$$\dot{Q} = -\sum_{\alpha=1}^{N_s} \Delta h^0_{f\alpha} \hat{\dot{\omega}}_\alpha = -\sum_{\alpha=1}^{N_s}\sum_{j=1}^{N_r} \Delta h^0_{f\alpha} (\nu''_{j\alpha} - \nu'_{j\alpha}) \dot{\omega}_j. \tag{3.1}$$

Here N_r represents the number of reactions in the chemical mechanism, $\nu'_{j\alpha}$ and $\nu''_{j\alpha}$ are respectively the reactant-side and product-side stoichiometric coefficients associated to species α and reaction j, $\Delta h^0_{f\alpha}$ is the enthalpy of formation of species α at standard conditions, $\dot{\omega}_j$ is the reaction rate of reaction j and $\hat{\dot{\omega}}_\alpha$ is the production rate of species α. The acoustic source term in (1.1) can therefore be written as

$$\frac{\partial \dot{Q}}{\partial t} = \sum_{j=1}^{N_r} \frac{\partial \dot{Q}_j}{\partial t} = -\sum_{\alpha=1}^{N_s}\sum_{j=1}^{N_r} (\nu''_{j\alpha} - \nu'_{j\alpha}) \Delta h^0_{f\alpha} \frac{\partial \dot{\omega}_j}{\partial t}, \tag{3.2}$$

where $\dot{Q}_j$ denotes the heat release rate associated with reaction j. Equation (3.2) explicitly shows that the rate of change of reaction rates $\partial\dot{\omega}_j/\partial t$ has a direct impact on $\partial\dot{Q}/\partial t$ and, therefore, on the generated sound. The term $\partial\dot{Q}/\partial t$ can be related to the fluctuations of the heat release rate $\dot{Q}'$ by a time scale τ_1 such that the following relationship for the acoustic power can be established:

$$\overline{p'^2} \propto \overline{\left(\int \partial\dot{Q}/\partial t \,\mathrm{d}V\right)^2} = \frac{1}{\tau_1^2}\overline{\left(\int \dot{Q}' \,\mathrm{d}V\right)^2}. \tag{3.3}$$

Here the overline denotes temporal averaging. Equation (3.3) will be used in § 4.3 to examine the impact of heat release rate fluctuations on the generated sound. A similar approach was used by Swaminathan *et al.* (2011) to model the overall acoustic sound pressure level (OASPL) of turbulent premixed flames. Following a reasoning analogous to their study, a further decomposition of $\dot{Q}' = \dot{Q} - \bar{\dot{Q}}$ shows that $\partial\dot{Q}/\partial t$ can also be related to the heat release rate using a different time scale τ_2,

$$\overline{p'^2} \propto \overline{\left(\int \partial\dot{Q}/\partial t \,\mathrm{d}V\right)^2} = \frac{1}{\tau_2^2}\overline{\left(\int \dot{Q} \,\mathrm{d}V\right)^2}. \tag{3.4}$$

Note that the time scales τ_1 and τ_2 have different physical interpretations. While τ_1 indicates how effectively fluctuations of the heat release rate produce sound, τ_2 shows how effectively heat is converted to sound. By extending (3.4) to individual reactions using a time scale $\tau_{2,j}$, the contribution of reaction j to the generated sound can be estimated as

$$\overline{p'^2} \propto \sum_{j=1}^{N_r}\left[\frac{1}{\tau_{2,j}^2}\overline{\left(\int \dot{Q}_j \,\mathrm{d}V\right)^2} + \sum_{k=1,\ k\neq j}^{N_r} \overline{\int \frac{\partial\dot{Q}_j}{\partial t}\,\mathrm{d}V \int \frac{\partial\dot{Q}_k}{\partial t}\mathrm{d}V}\right]. \tag{3.5}$$

The first term in the square brackets denotes the contribution of reaction j only while the second term represents the cross-contribution of reactions j and k. Equations (3.4) and (3.5) will be used in § 4.3 to analyse the relative contribution of different reactions to combustion noise.

3.2. *Relationship between flame stretch and combustion noise*

According to Tam *et al.* (2019), a mechanistic theory relating flame front dynamics to sound generation can shed light on the sources of combustion noise. Such a framework is provided by (1.3). The flame stretch, noted as κ, represents the local change of the flame surface area,

$$\kappa = \frac{1}{\delta A}\frac{\mathrm{d}(\delta A)}{\mathrm{d}t}, \tag{3.6}$$

where δA represents an infinitesimal portion of the flame surface. The overall $\mathrm{d}A/\mathrm{d}t$ can therefore be written as

$$\frac{\mathrm{d}A}{\mathrm{d}t} = \frac{\mathrm{d}}{\mathrm{d}t}\int_A \delta A = \int_A \frac{\mathrm{d}(\delta A)}{\mathrm{d}t} = \int_A \kappa \delta A, \tag{3.7}$$

so that (1.3) can be expressed as

$$p'(r_s, t) = \frac{\rho_\infty S_L}{4\pi r_s}\left(\frac{\rho_u}{\rho_b} - 1\right)\left[\int_A \kappa \delta A\right]_{t - r_s/c_\infty}. \tag{3.8}$$

The flame stretch rate can be expressed as the sum of a dilatation term (κ_D), a normal strain rate term (κ_N) and a curvature term (κ_C) (Matalon 1983; Candel & Poinsot 1990), i.e.

$$\kappa = \kappa_D + \kappa_N + \kappa_C = \frac{\partial u_i}{\partial x_i} - n_i n_j \frac{\partial u_i}{\partial x_j} + S_d \frac{\partial n_i}{\partial x_i}, \tag{3.9}$$

where S_d is the local flame displacement speed and $\boldsymbol{n}$ is the unit flame normal vector pointing towards the unburnt mixture. The positive values of κ represent flame surface generation while negative values indicate flame surface destruction. The term $\partial n_i/\partial x_i$ in (3.9) represents the flame surface curvature. This term will be negative when the flame is curved towards the unburnt gases and positive when curved towards the burnt gases. Markstein (1964) developed what is known as Markstein linear theory, relating the flame displacement speed to flame curvature as

$$\frac{S_d}{S_L} = 1 - l_M \nabla \cdot \boldsymbol{n}, \tag{3.10}$$

where the proportionality constant, l_M, is known as the Markstein length. Equation (3.10) is a simple framework that has been extensively examined in the literature. For instance, Peters *et al.* (1998) and Peters (1999) also derived a linear relationship between S_d and curvature to model flames in the thin-reaction zone with the G-equation, and verified the validity of the formulation using DNS of two-dimensional (2-D) unsteady methane/air flames. Recently, Dave & Chaudhuri (2020) studied the behaviour of S_d in a turbulent hydrogen/air flame featuring flame annihilation events, which are characterised by large negative curvatures and large stretch. They showed that a linear relationship between S_d and curvature can be used for these annihilation events. In addition, Trivedi *et al.* (2019) used Morse theory to show that S_d is linearly dependent on curvature during pocket formation.

In this framework of large curvature values, κ_D and κ_N become negligible so that $\kappa \simeq \kappa_C$. Under the assumption that Markstein linear theory holds, (3.8) and (3.10) can

be combined to express the far field noise as

$$p'(r_s, t) = \frac{\rho_\infty S_L^2}{4\pi r_s}\left(\frac{\rho_u}{\rho_b} - 1\right)\left[\int_A \nabla \cdot \boldsymbol{n}\,(1 - l_M \nabla \cdot \boldsymbol{n})\,\delta A\right]_{t - r_s/c_\infty}. \tag{3.11}$$

Equation (3.11) shows that the pressure fluctuations have a strong dependence to the flame surface curvature. Note that the S_L^2 acoustic dependence for spherically symmetric annihilation events demonstrated by Talei, Brear & Hawkes (2011) is retrieved here. Equation (3.11) will be used in § 4.4 to relate the flame dynamics to combustion noise.

4. Results and discussion

4.1. *Flame/turbulence interaction*

The progress variable C is defined based on the O_2 mass fraction, as commonly defined in DNS studies of premixed methane/air flames (Sankaran *et al.* 2007; Vreman *et al.* 2009; Thornber *et al.* 2011; Wang, Hawkes & Chen 2016),

$$C = \frac{Y_{O_2} - Y_{O_2,u}}{Y_{O_2,b} - Y_{O_2,u}}. \tag{4.1}$$

The progress variable is therefore zero in the unburnt mixture and unity in the fully burnt region. The unit flame normal vector $\boldsymbol{n}$ is defined as $\boldsymbol{n} = -\nabla C/|\nabla C|$ and the local curvature as $\nabla \cdot \boldsymbol{n}$. The instantaneous flame surface is defined based on the progress variable isosurface corresponding to the location of the maximum heat release rate in an unstrained 1-D laminar flame under the same conditions as the turbulent flames. This progress variable equals to 0.82 and 0.62 for the BFER and COFFEE cases, respectively.

The instantaneous flame surface of the two cases, coloured with the absolute value of the flame surface curvature, are shown in figure 4. As pointed out by the ellipses in the left panels, both flames have similar features close to the inlet. This similarity is expected as the boundary conditions at the inlet are the same. However, the flame surfaces become increasingly different further downstream, showing that the kinetics impact the flame dynamics. The COFFEE flame appears more wrinkled and features more detached pockets of unburnt mixture. As discussed in previous studies (Rajaram & Lieuwen 2009; Haghiri *et al.* 2018), most of the acoustic sources are concentrated around the flame tip. Therefore, the difference between the two flames in that region can lead to different far field noise, as it will be discussed in § 4.4.

In cylindrical coordinates the flame surface normal is written as $\boldsymbol{n} = [n_x, n_r, n_\theta]$, where n_x, n_r and n_θ represent the flame normal components in the streamwise, radial and azimuthal directions, respectively. To investigate the orientation of the flame surface, the probability density functions (PDFs) of $\boldsymbol{n}$ are shown in the left panels of figure 5. Close to the inlet (at $x/D = 2$), the flames have the same orientation, consistent with figure 4. The preferred value for the radial orientation is -1, while the preferred value for the streamwise and azimuthal components is close to 0, meaning that the orientation is similar to that of the cylindrical laminar flame imposed at the inlet. Further downstream, at $x/D = 10$, the radial and azimuthal PDFs are still similar. These distributions are very broad, with no preferred orientation and, therefore, feature a PDF value around 0.5. The streamwise PDFs are slightly different between the two cases in the upper half of the flame. The maximum PDF value occurs at $n_x = 0$ for the BFER case, meaning that the flame will tend to be parallel to the streamwise jet centreline. On the other hand, the COFFEE flame has an orientation with less preference to any direction, consistent with the higher level of wrinkling observed earlier.

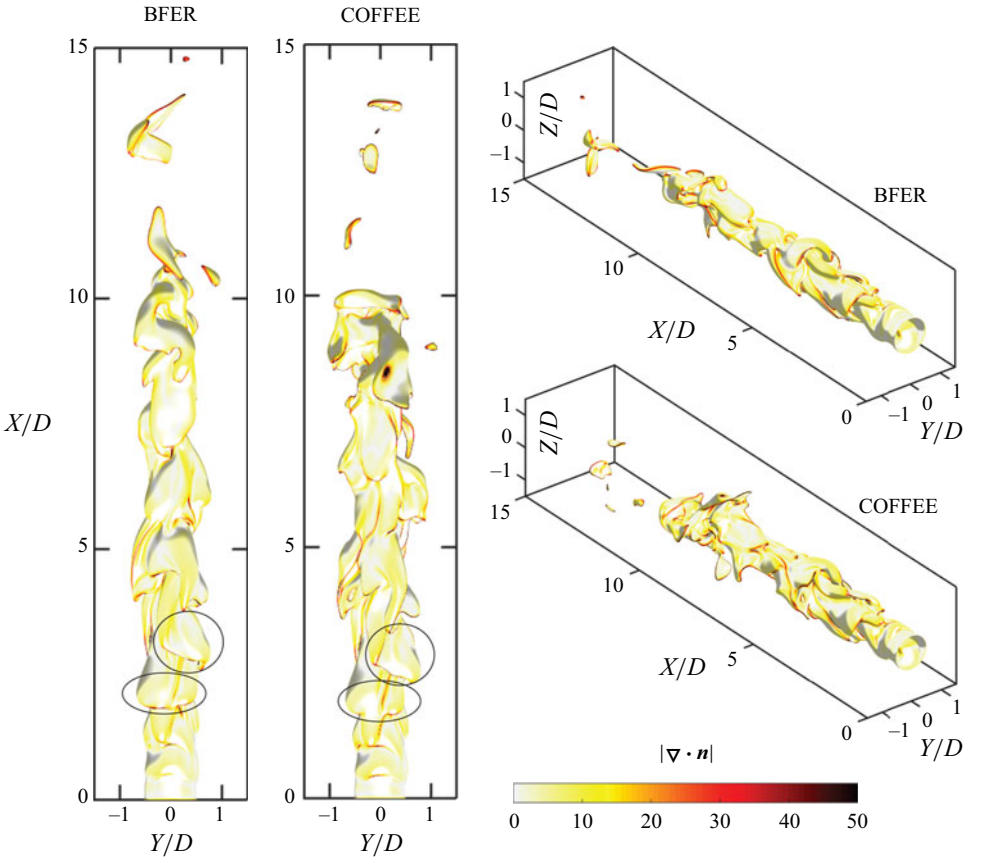

Figure 4. Instantaneous isosurfaces of progress variable $C = 0.82$ and $C = 0.62$ for the BFER and COFFEE flames, respectively, coloured by the flame curvature magnitude.

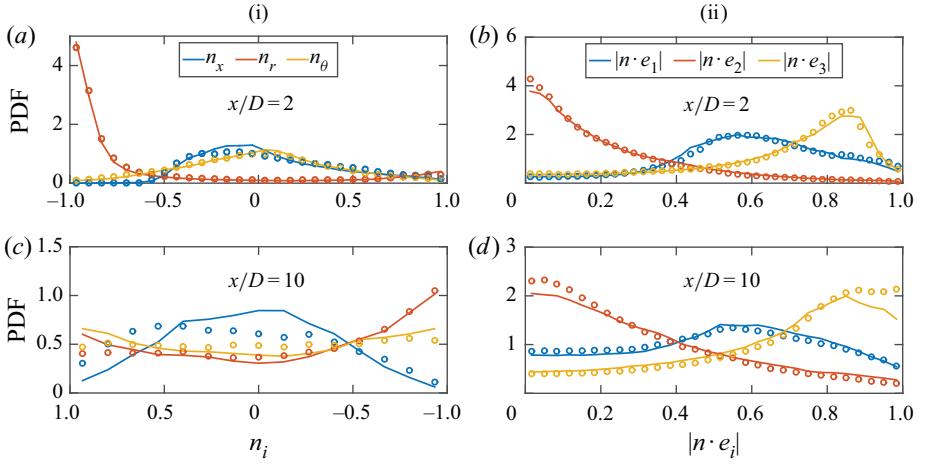

Figure 5. Probability density functions of (i) the flame normal $\boldsymbol{n}$ components and (ii) the flame normal strain rate alignment $|\boldsymbol{n} \cdot \boldsymbol{e}_i|$ for the BFER (solid lines) and COFFEE (hollow markers) cases, at streamwise locations $x/D = 2$ (*a*,*b*) and $x/D = 10$ (*c*,*d*).

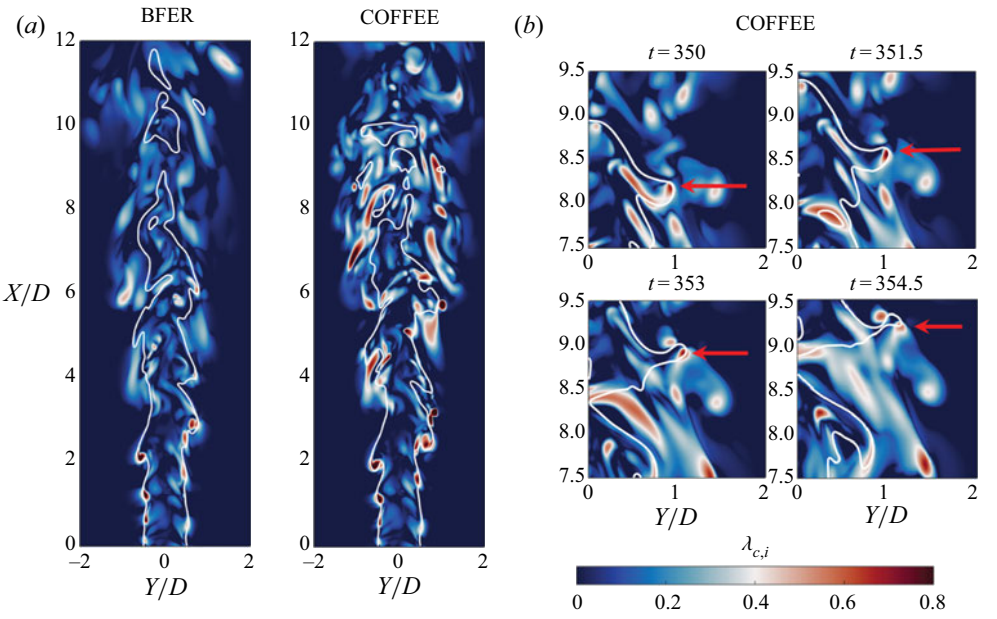

Figure 6. (*a*) Instantaneous swirling strength $\lambda_{c,i}$ and flame surface (white line) on the central *XY* plane for the BFER and COFFEE cases. (*b*) Detailed view picturing the temporal evolution of a vortex/flame interaction in the COFFEE case.

We now analyse flame/turbulence interaction to further examine and explain the differences between the two cases. The right panels in figure 5 show the PDFs related to the alignment between the flame normal and the strain rate eigenvectors $\boldsymbol{e}_i$, which is characterised by the absolute value of the cosine angle between the vectors, i.e. $|\boldsymbol{n} \cdot \boldsymbol{e}_i|$. The eigenvectors $\boldsymbol{e}_1$ and $\boldsymbol{e}_3$ represent the most extensive and most compressive strain rates, respectively. The distributions show that the flames tend to align preferentially with $\boldsymbol{e}_3$ at downstream locations, consistent with the results of Ma, Talei & Sandberg (2020) for a similar Karlovitz number flame. Additionally, Baum *et al.* (1994) reported a preferential alignment between $\boldsymbol{n}$ and $\boldsymbol{e}_3$ regardless of whether reduced or complex chemistry was used. The similarity between the BFER and COFFEE PDFs confirms this, implying that the flame-flow alignment is not dependent on the chemical modelling.

Figure 6(*a*) shows the instantaneous swirling strength $\lambda_{c,i}$ and the flame surface at the central XY plane for both cases. Animations are provided as supplementary material available at https://doi.org/10.1017/jfm.2020.1184. The swirling strength is the imaginary part of the complex eigenvalues of the velocity gradient tensor (Zhou *et al.* 1999). The swirling strength is commonly used to identify vortical structures and has the advantage of being insensitive to the mean shear stress, contrary to vorticity. As expected, the vortical structures are very similar close to the inlet. The flame front tends to wrap around the vortices in the shear layer, creating typical flame cusps, as those seen around $x/D = 2$. In the BFER case the vortices present in the shear layer decay more rapidly with increasing streamwise location compared with the COFFEE case, where strong swirling motions are still found around $x/D = 6$ both in the unburnt and burnt gas regions. It indicates that chemical modelling can have an impact on the turbulence, even for flames with Karlovitz numbers which are an order of magnitude larger than unity.

Furthermore, a detailed inspection of several snapshots of vortex/flame interactions reveals that the vortices still deform the flame front in the upper-half of the COFFEE flame.

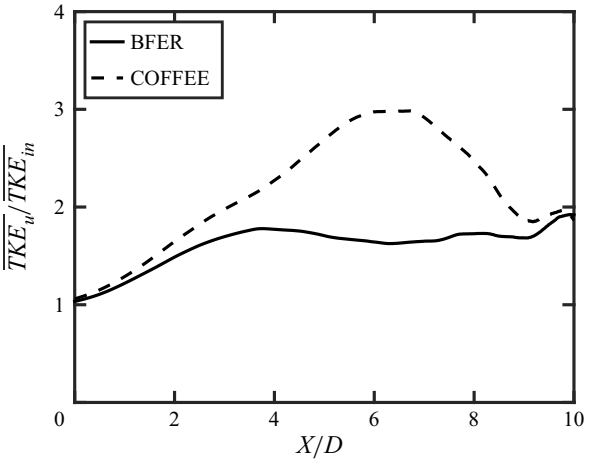

Figure 7. Temporal mean of the TKE in the unburnt gases at the centreline.

In the panels displayed in figure 6(*b*), representing the COFFEE case, the vortex of interest (highlighted by the red arrow) stretches the flame, leading to a highly curved flame which eventually causes flame annihilation. This shows that the different flow dynamics in the unburnt region lead to different flame dynamics around the flame tip.

To further quantify the impact of chemical modelling on the flow field, the temporal mean of the turbulent kinetic energy (TKE) in the unburnt mixture (noted $\overline{\mathrm{TKE}}_u$) at the jet centreline is shown in figure 7. This quantity was obtained by conditioning the computation of the TKE to values of the progress variable lower than a threshold $C^+ = 0.05$ as

$$\mathrm{TKE}_u = \tfrac{1}{2}\left(u'_{i,u}\right)^2 = \tfrac{1}{2}\left(u_i\,|_{C<C^+} - \overline{u_i\,|_{C<C^+}}\right)^2, \tag{4.2}$$

where $u'_{i,u}$ denotes the u_i r.m.s., conditioned in the unburnt region. For a point in the flame brush oscillating between unburnt and burnt gases, the velocity jump across the flame front leads to large TKE values, which are not representative of the turbulence level in the flow (Poinsot & Veynante 2005, p. 186–187). The conditioning used in (4.2) removes these effects when computing the velocity fluctuations (Shepherd, Moss & Bray 1982; Cheng 1984).

Figure 7 shows that using different chemical mechanisms leads to very different $\overline{\mathrm{TKE}}_u$ in the region $4 < x/D < 8$, where the flow is more turbulent in the COFFEE flame. It is worth noting that the impact of flame on turbulence in the unburnt region has been reported in the literature (Furukawa *et al.* 2002; Steinberg, Driscoll & Ceccio 2008). As it will be shown in § 4.3, the BFER case features a significantly higher heat release rate peak, which will increase the magnitude of the viscous dissipation term and the mean dilatation term in the TKE budget equation (Zhang & Rutland 1995). The higher amplitude of these sink terms is expected to dampen turbulence more strongly.

The flame structure is another feature that is affected by turbulence. The surface density function $|\nabla C|$, which is representative of the inverse of the local flame thickness, can be used to assess how turbulence impacts the flame structure. Figure 8 shows the conditionally averaged $|\nabla C|$ on C for both cases, at several streamwise locations. The results from the unstrained laminar flame imposed at the inlet are also shown by the dashed lines. In the BFER case the flame becomes initially slightly thinner before thickening further downstream. However, the overall flame structure remains close to

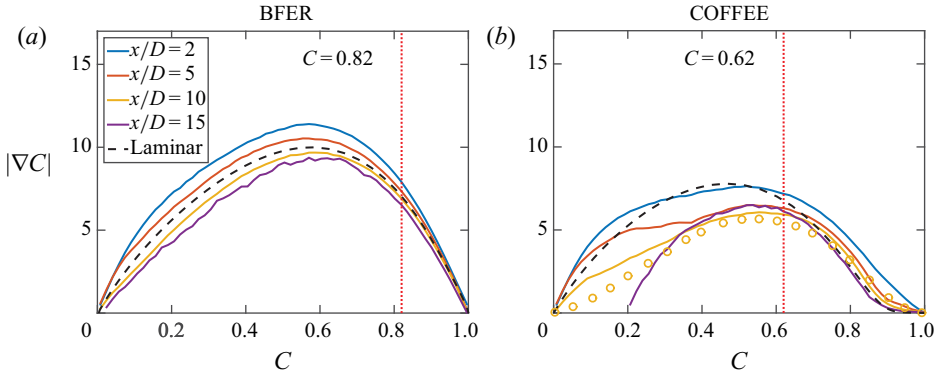

Figure 8. Surface density function $|\nabla C|$ conditionally averaged on the progress variable C for different streamwise locations. The progress variable value corresponding to the flame surface is represented by the dotted red line and results from Sankaran *et al.* (2007) are represented by hollow circles.

that of the laminar flame. With the COFFEE mechanism, a significant thickening occurs in the preheat region ($0.2 < C < 0.6$) for $x/D > 5$. This result is expected for a flame in the thin-reaction zone and matches with the results from Sankaran *et al.* (2007) for a preheated, lean, turbulent methane/air slot flame with a skeletal quasi-steady state chemistry mechanism. Note that the Karlovitz number is lower in the BFER case, due to the thinner flame obtained with this mechanism. It is therefore not surprising to observe a weaker impact of turbulence on the flame structure in this case. In addition, this result is consistent with previous studies pointing the reduced sensitivity of simple or semi-global chemistry flames to strain (Baum *et al.* 1994).

4.2. *Combustion noise*

To compare both flames in terms of acoustics, the pressure traces at $[x, y, z] = [15D, 8D, 0D]$ are used since this point is reasonably far from both the inlet and the flame. A power spectral density estimate S is obtained using Welch's method (Welch 1967) with six Hanning windows and a 50 % overlap. The result is normalised and converted to the sound pressure level (SPL) spectra,

$$\mathrm{SPL}(St) = 10\log\left(\frac{S_{p'p'}}{S_0}\right), \tag{4.3}$$

where S_0 is a reference power spectral density amplitude, taken as the maximum $S_{p'p'}$ value in the BFER case. The resulting SPL spectra are shown in figure 9, as a function of the Strouhal number, defined as $St = fD/\bar{u}_{in}$, where f represents the frequency.

The peak SPL values occur at $St = 0.16$ and $St = 0.27$ for the BFER and COFFEE cases, respectively. The acoustic peak for the COFFEE case is 3 dB lower than that of the BFER case. The biggest differences, however, occur in the frequency range $1 < St < 5$, where the COFFEE spectrum typically has a 10 dB greater SPL.

The OASPL is defined as

$$\mathrm{OASPL} = 10\log\left(\int \frac{S_{p'p'}(f)}{S_0}\mathrm{d}f\right) = 20\log\left(\frac{p'_{rms}}{p_0}\right), \tag{4.4}$$

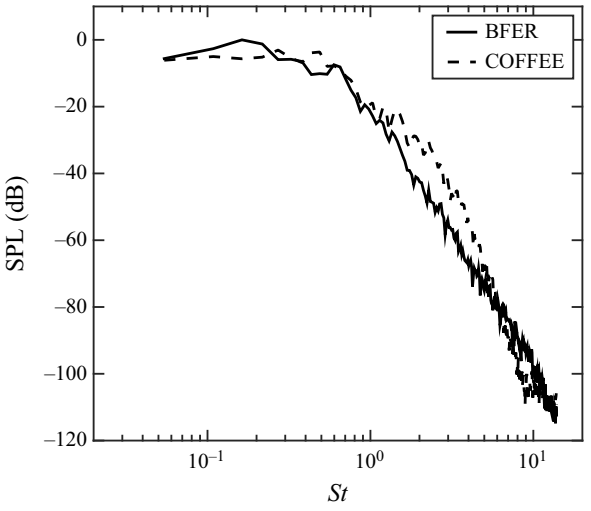

Figure 9. Pressure spectra at the location $[x, y, z] = [15D, 8D, 0]$ for the BFER (solid line) and COFFEE (dashed line) cases.

where p_0 represents a reference pressure level, and is 3.5 dB larger in the BFER case. This corresponds to approximately a 50 % difference in p'_{rms} and is illustrated by the different SPL at low frequencies, which contains most of the acoustic energy.

The assumption that $\partial\dot{Q}/\partial t$ is the dominant source of noise is now examined. *A posteriori* pressure traces at the location $[x, y, z] = [15D, 8D, 0D]$ are computed from the acoustic source term $\partial\dot{Q}/\partial t$, using a discretised form of (1.1). A more detailed description of the method can be found in Brouzet *et al.* (2019). The DNS and *a posteriori* pressure traces and spectra are shown in figure 10. The pressure fluctuations from DNS and those generated by $\partial\dot{Q}/\partial t$ have a correlation coefficient above 0.8 for both cases. Considering the spectra reveals that $\partial\dot{Q}/\partial t$ is clearly the dominant source of noise up to $St = 5$. The discrepancy observed for low SPL amplitudes at very high frequencies is believed to arise from the temporal interpolation of the acoustic source term $\partial\dot{Q}/\partial t$ at time $t - r_s/c_\infty$. Considering the importance of $\partial\dot{Q}/\partial t$ on the generated sound, the impact of chemical modelling on $\dot{Q}$ and $\partial\dot{Q}/\partial t$ is analysed in the next section.

4.3. *Impact of chemical modelling on $\dot{Q}$ and $\partial\dot{Q}/\partial t$*

The time-averaged temperature fields of both cases are displayed in the left panels of figure 11. The slower post-flame reactions present in the skeletal COFFEE mechanism still release a significant amount of heat for $x/D > L_{flame}$, resulting in a slow but gradual temperature increase in that region. As discussed in § 3.1, the acoustic power can be estimated using the r.m.s. of the volume integrated heat release rate fluctuations (3.3). Figure 11(*b*) shows that most of the heat release rate fluctuations arise from the flame brush. Indeed, inspection of the COFFEE case reveals that the heat release rate fluctuations in the post-flame region are typically one to two orders of magnitude lower than in the flame brush, suggesting that the post-flame region has negligible contributions to the generated sound.

The time scale τ_1 that relates $\dot{Q}'$ to the acoustic source term $\partial\dot{Q}/\partial t$ was computed using (3.3), and was equal to 5.1 and 5.2 time units for the BFER and COFFEE cases, respectively. This means that the difference in the acoustic power can be directly estimated

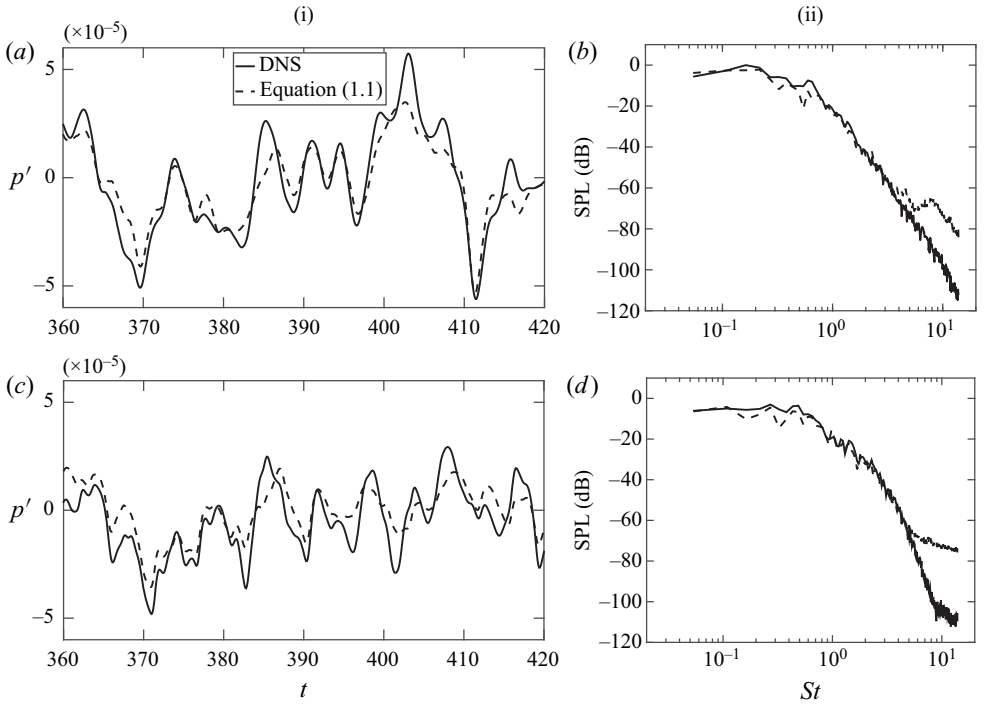

Figure 10. (i) Pressure traces and (ii) pressure spectra at the location $[x, y, z] = [15D, 8D, 0]$ directly extracted from the DNS (solid lines) and computed from $\partial\dot{Q}/\partial t$ with (1.1) (dashed lines) for the BFER (*a*,*b*) and COFFEE (*c*,*d*) cases.

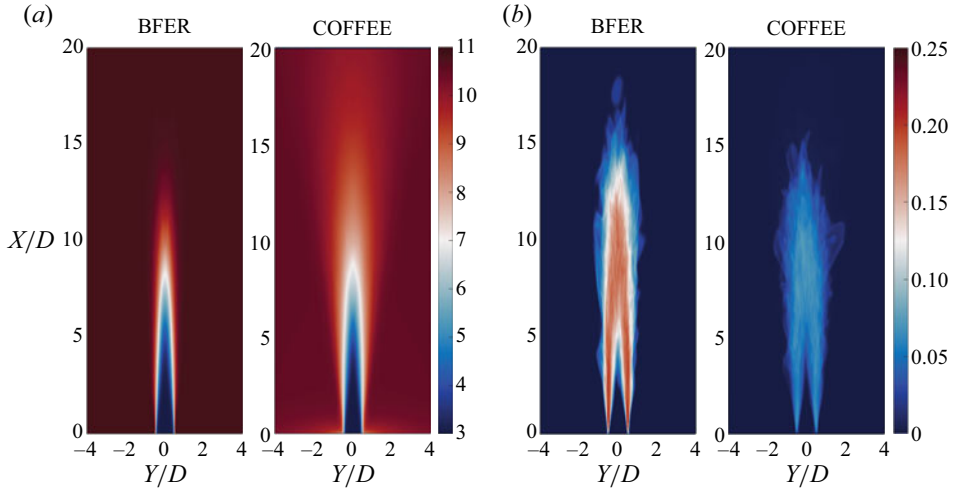

Figure 11. (*a*) Temporally averaged temperature and (*b*) r.m.s. of the heat release rate fluctuations on the central XY plane.

by comparing the integrated fluctuations of the heat release rate. The r.m.s. value of the volume integrated $\dot{Q}'$ is larger by 60 % in the BFER case, consistent with the OASPL difference previously observed in § 4.2. In addition, the time scale τ_2 relating $\dot{Q}$ to $\partial\dot{Q}/\partial t$, computed with (3.4), is significantly larger in the COFFEE case, meaning that

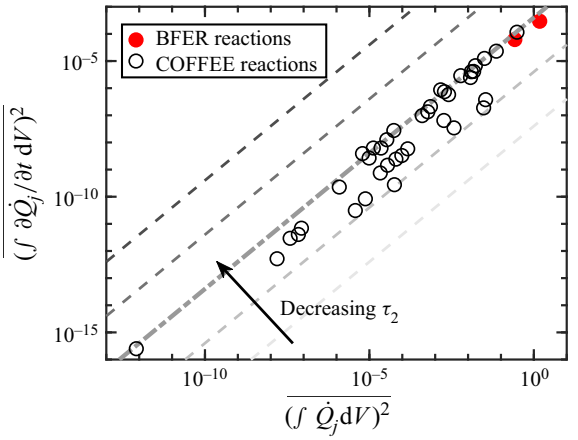

Figure 12. Scatter plot of $\overline{(\int \dot{Q}_j \,\mathrm{d}V)^2}$ and $\overline{(\int \partial\dot{Q}_j/\partial t \,\mathrm{d}V)^2}$ for the reactions in the BFER and COFFEE mechanisms. The dashed lines represent constant τ_2 values. The dotted–dashed line represents the time scale $\tau_{flame} = L_{flame}/U_{bulk} \approx 50$ time units.

the COFFEE mechanism will produce smaller fluctuations of the heat release rate. The remainder of this section aims at exploring the reasons leading to this $\dot{Q}'$ discrepancy.

Equation (3.5) is now used to examine the contribution of individual reactions to the overall generated sound. Figure 12 shows how efficient a given reaction is at converting heat into sound. The dashed lines show the following relationship using different values of τ_2:

$$\overline{\left(\int \partial\dot{Q}/\partial t \,\mathrm{d}V\right)^2} = \frac{1}{\tau_2^2}\overline{\left(\int \dot{Q}\,\mathrm{d}V\right)^2}. \tag{4.5}$$

Since this figure is shown using a log-log scale, all dashed lines have a slope of 1. The higher the line is, the faster the reaction is, meaning that it is more efficient at converting heat into sound. The dotted–dashed line represents the flame time scale τ_{flame} defined as the ratio of the mean flame length to the inlet bulk velocity $L_{flame}/U_{bulk} \approx 50$ time units. This time scale therefore represents the average time taken by a reactant molecule to reach the flame tip, where it will be consumed. It is not surprising to note that τ_{flame} features a value very close to the time scale $\tau_{2,j}$ of the dominant and most efficient reactions.

In addition, it is observed that the two reactions in the BFER mechanism feature a similar time scale $\tau_{2,j}$, close to τ_{flame}. However, a wide range of time scales is found in the COFFEE mechanism, spreading from 40 time units ($HCO + O \Leftrightarrow CO + OH$) to 450 time units ($HO_2 + CO \Leftrightarrow CO_2 + OH$) and illustrating the variety of reactions that are modelled in this mechanism. These acoustically less efficient reactions explain the higher overall τ_2 time scale of the COFFEE flame.

Further examination of the results presented in figure 12 showed that the acoustically dominant reaction for each mechanism was the most exothermic reaction,

$$CH_4 + 1.5O_2 \Rightarrow CO + 2H_2O \quad \text{(BFER)}, \tag{4.6}$$

$$CH_3 + O \Leftrightarrow CH_2O + H \quad \text{(COFFEE)}. \tag{4.7}$$

Using (3.2), the contribution of every reaction to the overall $\partial\dot{Q}/\partial t$ is computed. Figure 13 demonstrates the contribution of the acoustically dominant reaction to the total $\partial\dot{Q}/\partial t$, which accounted for 70 % of the total $\int \partial\dot{Q}/\partial t \,\mathrm{d}V$ r.m.s. The high correlation

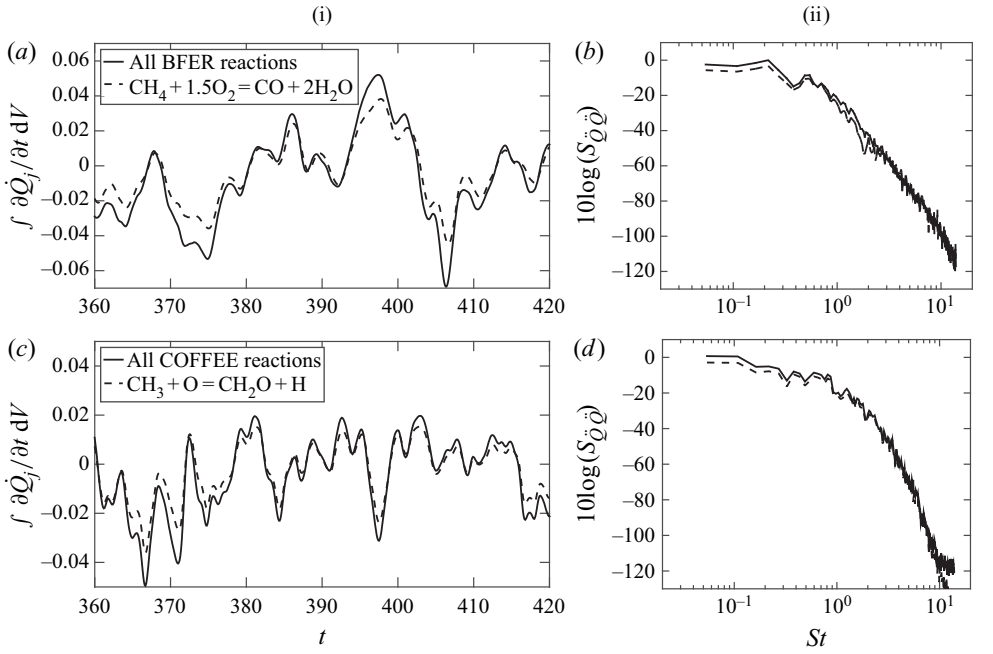

Figure 13. (i) Temporal evolution and (ii) corresponding power spectral densities of the volume integral of $\partial\dot{Q}/\partial t$ for all the reactions (solid lines) and the most exothermic reaction (dashed lines) in the BFER (*a*,*b*) and COFFEE (*c*,*d*) cases.

between the two terms is also evident. A 3 dB difference is observed at the lowest frequencies while there are no significant differences for $St > 1$.

Figure 14 compares the heat release rate profiles of the most exothermic reactions of both mechanisms, in a 1-D freely propagating laminar flame. The most exothermic reaction has by far the largest contribution to the overall heat release rate compared with other reactions. The heat release rate peak of the dominant reaction, noted $\dot{Q}_{d,max}$, is approximately 65 % of the overall heat release rate peak $\dot{Q}_{max}$, for both mechanisms. The ratio $\dot{Q}_{d,max}/\dot{Q}_{max}$ has a similar value to the ratio

$$\int \frac{\partial \dot{Q}_d}{\partial t} \mathrm{d}V \Big/ \int \frac{\partial \dot{Q}}{\partial t} \mathrm{d}V \approx 0.70, \tag{4.8}$$

in the turbulent cases. This corroborates a scaling by Strahle (1985), who argued that $p' \propto \dot{Q}_{max}$. A higher $\dot{Q}_{max}$ obtained with the BFER mechanism is consistent with the larger fluctuations of the heat release rate for this case, observed in figure 11. This, in turn, leads to the OASPL discrepancy previously noted. It is therefore essential for a chemical mechanism to accurately model the heat release rate profile and its peak for a correct prediction of the overall acoustic power.

4.4. *Impact of stretch on combustion noise*

The preceding section showed the importance of the heat release rate profile in determining the overall sound amplitude. We now consider flame/turbulence interaction in order to explain the observed differences at high frequencies in the acoustic spectra (figure 9). We first analyse the flame stretch and the stretch terms displayed in (3.9). Then, we relate stretch to combustion noise using the theory presented in § 3.2.

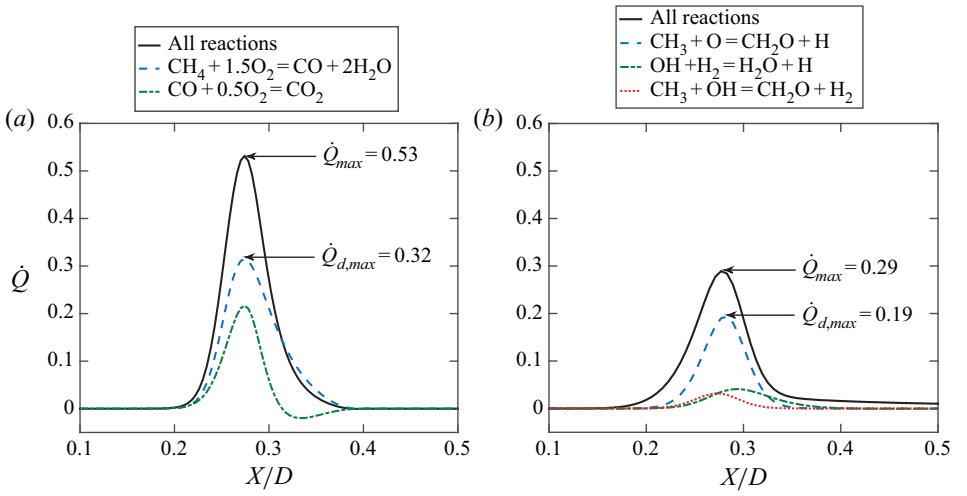

Figure 14. Total heat release rate (solid black line) and heat release rate of the most exothermic reactions for a 1-D freely propagating flame using the BFER (*a*) and COFFEE (*b*) mechanisms. The peaks of the total heat release rate and the most exothermic reaction are denoted by $\dot{Q}_{max}$ and $\dot{Q}_{d,max}$, respectively.

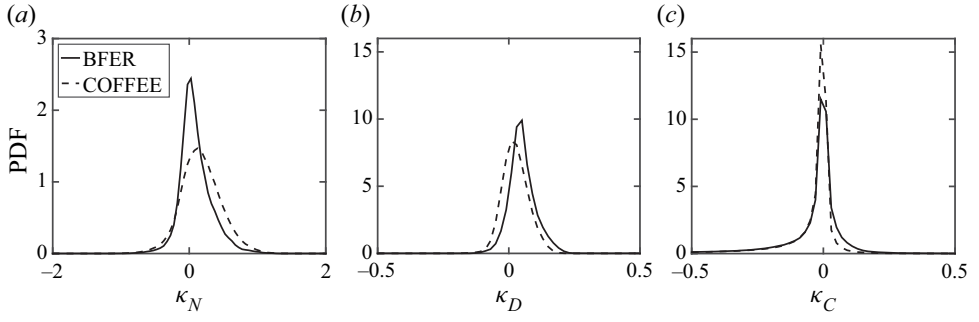

Figure 15. Probability density functions of the (*a*) normal strain rate, (*b*) dilatation and (*c*) curvature terms of the flame stretch rate (3.9).

The PDFs of the different stretch terms are compared between the two cases in figure 15. The κ_N distribution is broader in the COFFEE flame and is skewed towards higher positive values. This shows that the flame with the more complex chemistry is more sensitive to the surrounding flow strain, in accordance with a result found by Baum *et al.* (1994) for 2-D turbulent H_2 flames. The PDFs displayed in figure 15(*b*) show that κ_D values are small compared with κ_N. Considering the scaling used in the literature for this term (Chakraborty & Swaminathan 2007; Wang *et al.* 2016),

$$\kappa_D \simeq \frac{\Delta T}{T_u}\frac{S_L}{\delta_{th}}, \tag{4.9}$$

the magnitude of κ_D is about 0.1, which is consistent with the results presented here. Finally, the κ_C PDFs reveal that the curvature term has a tendency towards negative values in both cases.

To further examine the relationship between strain and curvature contributions to stretch, the following theoretical argument is used. In a statistically stationary flame, the condition

$\overline{\mathrm{d}A/\mathrm{d}t} = 0$ translates into

$$\overline{\int_A \kappa_N \delta A} = -\overline{\int_A \kappa_C \delta A}, \tag{4.10}$$

where the dilatation term κ_D has been neglected. Equation (4.10) shows that higher positive κ_N values must be balanced by lower negative κ_C values. Indeed, the mean κ_C is 50 % lower in the COFFEE case, consistent with a higher mean κ_N for this case. This difference is the subject of a comprehensive analysis later in this section. Equation (4.10) illustrates the equilibrium between flame surface generation and destruction, which was exemplified in figure 6(*b*) where a heavily strained flamelet led to an annihilation event. It is therefore important to note that the discrepancy observed between the two cases in terms of flame wrinkling (in figure 4) is a consequence of the different flame response to the flow strain.

To establish under which conditions the normal strain rate and the curvature stretch terms are dominant, the joint PDFs are examined in figure 16. The white dashed line represents the conditionally averaged κ terms on the total stretch. For positive stretch values, a strong correlation is observed between κ_N and κ (*a*,*b*), indicating that flame straining in the normal direction to the flame front is the dominant mechanism for generation of flame surface area. On the other hand, κ_N values smaller than -0.5 are rare, indicating that strain does not significantly contribute to the destruction of the flame surface area. The joint PDF of the dilatation and global stretch (*c*,*d*) confirms that κ_D is negligible and has no correlation with κ.

The bottom row in figure 16 shows that κ_C is dominant for values lower than -0.5. This is even clearer showing the full range of κ and κ_C in figure 17, which reveals an excellent correlation between these two quantities for highly negative values of stretch. To summarise, the normal strain and the curvature terms are dominant for $\kappa > 0$ and $\kappa < -0.5$, respectively. However, neither κ_N or κ_C are dominant for mildly negatively stretched flamelets ($-0.5 < \kappa < 0$).

As shown in our previous studies, destruction of the flame surface area plays a major role in terms of the generated sound, in particular for high frequencies (Haghiri *et al.* 2018; Brouzet *et al.* 2019). The focus is therefore placed on negative stretch values, when κ_C is dominant. To compare in greater detail the stretch PDFs between the BFER and COFFEE cases, logarithmic scales are used in figure 18(*a*). While the distributions are similar for low stretch values, they become increasingly different as the magnitude of stretch increases. In the range $1 < -\kappa < 20$, the stretch PDF of the COFFEE flame has an average value more than twice as high as that of the BFER flame.

According to (3.9), negative κ_C are associated with negative values of curvature, i.e. flame curved towards the unburnt gas (assuming that the flame displacement speed remains positive). The PDFs of positive S_d and negative $\boldsymbol{\nabla \cdot n}$ values are examined in figures 18(*b*) and 18(*c*) to understand how they affect the stretch statistics. When plotted on logarithmic scales, there is an insignificant difference between the flame displacement speed PDFs for $S_d/S_L > 10$, indicating that the higher occurrence of highly negative stretch in the COFFEE case is not due to large values of S_d. Inspection of the curvature PDFs shows however that highly curved flame regions ($-\boldsymbol{\nabla \cdot n} > 30$) are more present in the COFFEE case, confirming the qualitative observation from figure 4 that this flame is more wrinkled. To illustrate the highly curved surfaces, figure 19 shows a zoomed view of the COFFEE flame, coloured by the local value of curvature. Both elongated cusp regions and annihilation events, highlighted by the black and red circles, respectively, are found to feature highly curved surfaces.

Up to this point, the flame with a more complex chemistry was found to be more stretched and to feature more highly curved surfaces. As shown by (3.8) and (3.11), this

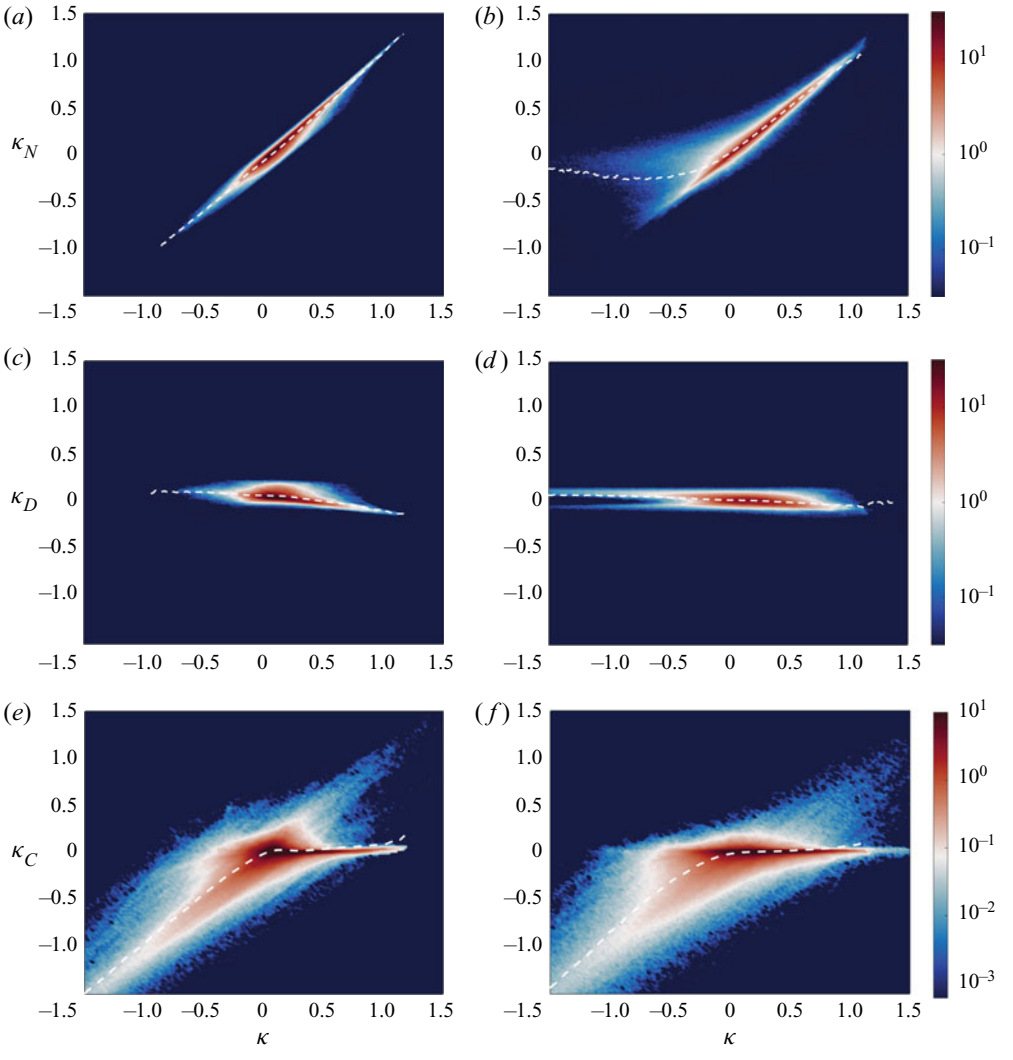

Figure 16. Joint PDFs of the flame stretch κ with its components κ_N (*a*,*b*), κ_D (*c*,*d*) and κ_C (*e*,*f*) for the BFER (*a*,*c*,*e*) and COFFEE (*b*,*d*,*f*) cases.

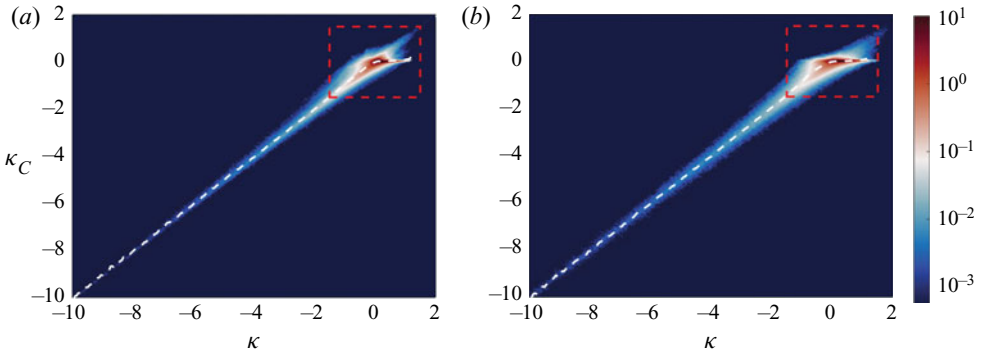

Figure 17. Expanded view of the joint PDFs of the flame stretch κ with κ_C for the BFER (*a*) and COFFEE (*b*) cases. The dashed boxes represent the extent of the views shown in figure 16.

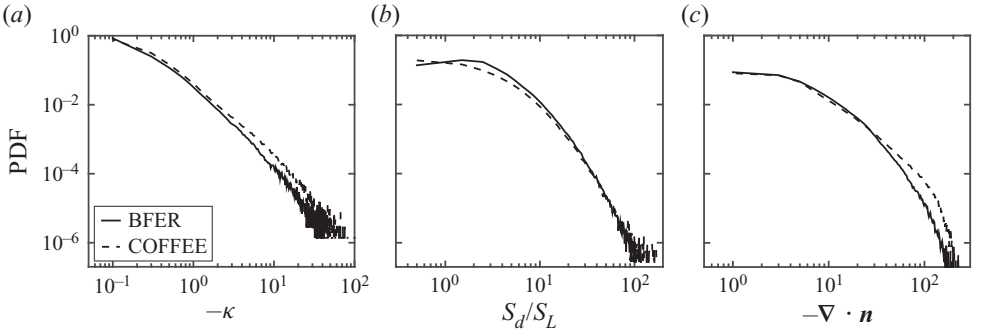

Figure 18. Probability density functions of the (*a*) flame stretch κ, (*b*) normalised flame displacement speed S_d/S_L and (*c*) curvature $\nabla \cdot \boldsymbol{n}$.

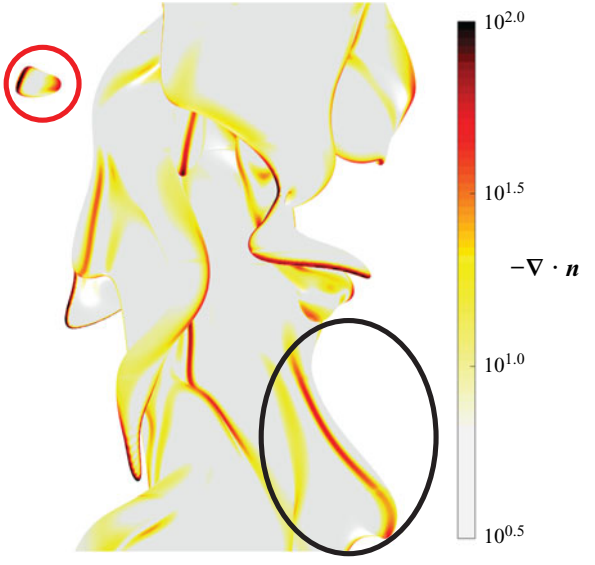

Figure 19. An instantaneous flame surface in the COFFEE case coloured with the flame curvature, showing elongated cusps (black ellipse) and flame annihilation (red circle).

should lead to different acoustic outputs between the two flames. To asses this, we first verify the validity of Markstein linear theory (3.10), which was used to derive (3.11). Figure 20 shows the joint PDFs of curvature and flame displacement speed for the two flames. The least-squares linear fit, considering $S_d/S_L > 0$ and $\nabla \cdot \boldsymbol{n} < 0$, is represented by the solid red line. Even though Markstein theory was developed for low curvature values, there is a strong dependency between S_d and $\nabla \cdot \boldsymbol{n}$ for a large range of curvatures, as also found by other studies (see § 3.2). The correlation coefficient between the two variables is 0.85, for both cases. The Markstein length extracted from the least-squares fit equals $l_M = 0.435$ and $l_M = 0.306$ for the BFER and COFFEE flames, respectively.

A scaling proposed by Strahle (1971) is now used to investigate the impact of curvature on the generated sound. He argued that the characteristic time scale τ_c associated with the flame motion is equal to the time of passage of a fluid element through the turbulent flame zone, i.e. $\tau_c \approx \delta_c/S_d$, where δ_c represents a characteristic flame thickness. Using this argument, a characteristic acoustic frequency f_c is defined based on the local flame

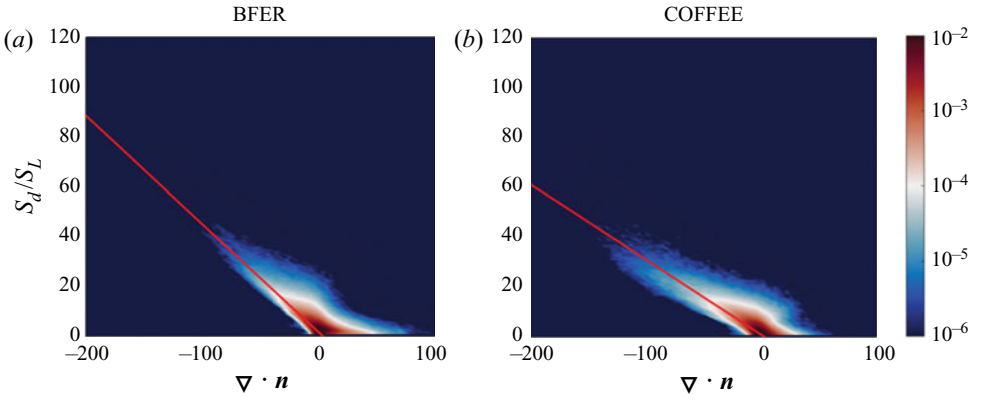

Figure 20. Joint PDFs of curvature and flame displacement speed for the BFER (*a*) and COFFEE (*b*) cases. The solid red lines represent the least-squares linear fit.

displacement speed so that $f_c \approx S_d/\delta_c$. As this scaling is used here to relate the flame motion to the generated sound, the characteristic flame thickness δ_c should be relevant to sound generation. The acoustically dominant reactions were therefore used to obtain δ_c, which is defined as the full width at tenth maximum of the dominant reaction heat release rate, leading to values of $\delta_c = 0.127$ and $\delta_c = 0.099$ for the BFER and COFFEE cases, respectively.

Using Markstein linear theory to relate S_d to $\nabla \cdot \boldsymbol{n}$, the following characteristic Strouhal number is then defined:

$$St_c = \frac{f_c D}{M} = \frac{S_d D}{\delta_c M} = \frac{(1 - l_M \nabla \cdot \boldsymbol{n}) S_L D}{\delta_c M}. \tag{4.11}$$

The PDF of curvature is established by considering a number of bins in the curvature space. According to (4.11), each bin has a unique characteristic Strouhal number. It is recalled that for large negative values of curvature, (3.11) shows that p' is a function of curvature only. One can therefore conclude that the pressure fluctuations spectrum in the far field must correlate with the curvature PDF. Assuming that the acoustic amplitude at the characteristic frequency St_c is proportional to the number of occurrences, the curvature PDF is converted to spectral space using (4.11).

Figure 21 shows the SPL spectra computed from the DNS p' (black lines) and the PDFs of $\nabla \cdot \boldsymbol{n}$ (red lines) which were converted to decibels by showing $20 \log_{10}(\text{PDF})$. The estimation from the curvature PDF shows a behaviour similar to the SPL spectra in the range $0.5 < St < 5$, retrieving the discrepancy between the two spectra at high frequencies. The mean difference between the BFER and COFFEE $20 \log_{10}(\text{PDF})$ curves is 12 dB in the range $1 < St < 5$, which is in accordance with the mean p' SPL difference in that range. The under-estimation for $St > 5$ and over-estimation for $St < 0.5$ are believed to arise, respectively, from the Markstein linear theory and the $\kappa \approx \kappa_C$ assumptions not to be valid anymore.

This modelling shows that the trend of the SPL acoustic spectrum in the high frequency range is proportional to the occurrence of highly curved flamelets and can be estimated using the curvature PDF. Furthermore, it shows that the discrepancy between the semi-global BFER mechanism and the more complex skeletal COFFEE chemistry arises from different flame dynamics and, more specifically, from more occurrences of highly curved flame surfaces in the latter case.

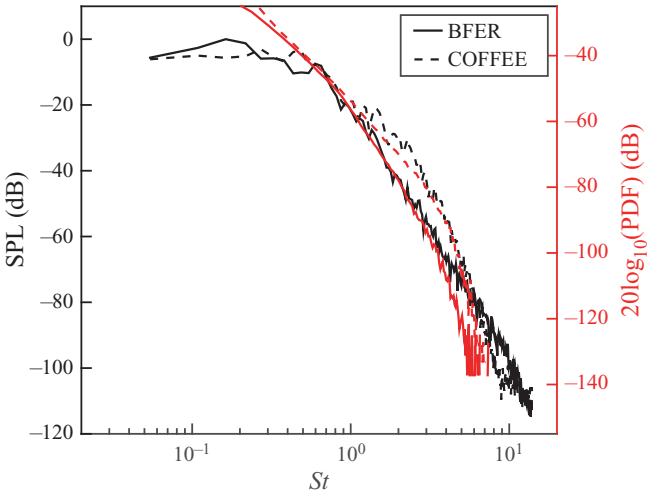

Figure 21. Sound pressure level spectra from DNS (black) and estimated from the flame curvature PDF (red) for the BFER (solid lines) and COFFEE (dashed lines) cases.

5. Conclusion

The impact of chemical modelling on the flame dynamics and sound generation by turbulent premixed methane/air jet flames was investigated using DNS. The semi-global BFER mechanism (Franzelli *et al.* 2012) and the more complex skeletal COFFEE mechanism (Coffee 1984) were used to perform these simulations.

It was first observed that these two chemical mechanisms resulted in similar flame structures close to the jet inlet. However, the flame modelled with the COFFEE mechanism was more wrinkled at downstream locations. Furthermore, the swirling strength and the TKE in the unburnt gases were higher with the COFFEE mechanism. These different dynamics indicate that the two-way coupling between the flame and turbulence depends on the choice of chemical mechanism.

The flame modelled with the COFFEE mechanism was also observed to have a significantly lower total acoustic power even though this case radiated more sound at high frequencies. The former result was due to this flame's smaller fluctuations in heat release rate, resulting from differences in the heat release rate profile. In both cases, the time derivative of the heat release rate $\partial\dot{Q}/\partial t$ was nonetheless the dominant acoustic noise source, as previous studies have shown, with the most exothermic reaction contributing to a substantial fraction of the generated sound.

The physical processes by which the COFFEE mechanism created greater acoustic content at high frequencies were then examined. Markstein's linear theory was first used to develop a model that related the acoustic spectrum to the PDF of the flame curvature. This demonstrated that this higher frequency acoustic content was the direct result of the COFFEE mechanism creating more wrinkled flame surfaces.

These results suggest that the accurate simulation of the noise emitted by turbulent premixed flames requires a chemical mechanism that ensures two main features. First, accurate modelling of the overall sound amplitude and the lower frequency acoustic spectra appears to require accurate modelling of the heat release rate profile in a 1-D sense. Second, accurate modelling of the acoustic spectrum at higher frequencies should first capture the flame/turbulence interaction. Whether a single, reduced order mechanism can address both priorities is not obvious, and will be considered further in future research.

Supplementary movies. Supplementary movies are available at https://doi.org/10.1017/jfm.2020.1184.

Funding. This work was supported by the Australian Research Council (ARC) [DE180100416] and the University of Melbourne through a Melbourne International Research Scholarship and a Melbourne International Fee Remission Scholarship. The research benefited from computational resources provided through the National Computational Merit Allocation Scheme and the Pawsey Energy and Resources Scheme, supported by the Australian Government. The computational facilities supporting this project included the Australian NCI National Facility and the Pawsey Supercomputing Centre.

Declaration of interests. The authors report no conflict of interest.

Author ORCIDs.
D. Brouzet https://orcid.org/0000-0003-1447-2538.

Appendix A. Chemical mechanisms

A.1. *Semi-global BFER mechanism*

Species	CH_4 O_2 CO_2 H_2O N_2 CO			
	Reactions	B^*	$\beta(-)$	E_a(cal gmol^{-1})
(1)	$CH_4 + 1.5O_2 \Rightarrow CO + 2H_2O$[1]	4.9×10^9	0.0	35 500
(2)	$CO + 0.5O_2 \Leftrightarrow CO_2$	2.0×10^8	0.8	12 000

The pre-exponential factors of the methane oxidation and the CO-CO_2 equilibrium reactions are adjusted by two correction functions depending on the local equivalence ratio and are given by Franzelli *et al.* (2012).
*Units of B involve gmol cm^{-3} and s.
[1]The forward reaction coefficients for this reaction are equal to 0.5 for CH_4 and 0.65 for O_2.

A.2. *Skeletal COFFEE mechanism*

Species	CH_4 CH_3 CH_2O HCO CO_2 CO H_2 H O_2 O OH HO_2 H_2O N_2			
	Reactions	B^*	$\beta(-)$	E_a(cal gmol^{-1})
(1)	$OH + H_2 \Leftrightarrow H_2O + H$	1.170×10^9	1.3	3626.3
(2)	$H + O_2 \Leftrightarrow OH + O$	1.420×10^{14}	0.0	16 393
(3)	$O + H_2 \Leftrightarrow OH + H$	1.800×10^{10}	1.0	8902
(4)	$H + O_2 + M \Leftrightarrow HO_2 + M$[1]	3.610×10^{17}	0.72	0
(5)	$H + HO_2 \Leftrightarrow 2OH$	1.400×10^{14}	0.0	1073
(6)	$H + HO_2 \Leftrightarrow O + H_2O$	1.000×10^{13}	0.0	1073
(7)	$H + HO_2 \Leftrightarrow H_2 + O_2$	1.250×10^{13}	0.0	0
(8)	$OH + HO_2 \Leftrightarrow H_2O + O_2$	7.500×10^{12}	0.0	0
(9)	$O + HO_2 \Leftrightarrow O_2 + OH$	9.1054×10^{12}	0.061	765.82

(10)	$H + H + H_2 \Leftrightarrow H_2 + H_2$	9.200×10^{16}	0.6	0
(11)	$H + H + N_2 \Leftrightarrow H_2 + N_2$	1.000×10^{18}	1.0	0
(12)	$H + H + O_2 \Leftrightarrow H_2 + O_2$	1.000×10^{18}	1.0	0
(13)	$H + H + H_2O \Leftrightarrow H_2 + H_2O$	6.000×10^{19}	1.25	0
(14)	$H + H + CO \Leftrightarrow H_2 + CO$	1.000×10^{18}	1.0	0
(15)	$H + H + CO_2 \Leftrightarrow H_2 + CO_2$	5.490×10^{20}	2.0	0
(16)	$CH_4 + H + H \Leftrightarrow CH_4 + H_2$	5.490×10^{20}	2.0	0
(17)	$H + OH + M \Leftrightarrow H_2O + M^2$	1.600×10^{22}	2.0	0
(18)	$H + O + M \Leftrightarrow OH + M^2$	6.200×10^{16}	0.6	0
(19)	$2OH \Leftrightarrow O + H_2O$	5.750×10^{12}	0.0	775
(20)	$CO + OH \Leftrightarrow CO_2 + H$	1.500×10^{7}	1.3	−765
(21)	$CO + O + M \Leftrightarrow CO_2 + M^1$	5.400×10^{15}	0.0	4570
(22)	$CO + H + M \Leftrightarrow HCO + M^1$	5.000×10^{14}	0.0	1500
(23)	$CH_4 + O \Leftrightarrow OH + CH_3$	4.070×10^{14}	0.0	13 988
(24)	$CH_4 + H \Leftrightarrow CH_3 + H_2$	7.240×10^{14}	0.0	15 081
(25)	$CH_4 + OH \Leftrightarrow H_2O + CH_3$	1.550×10^{6}	2.13	2444
(26)	$CH_4 + M \Leftrightarrow CH_3 + H + M^1$	4.680×10^{17}	0.0	93 210
(27)	$CH_3 + O \Leftrightarrow CH_2O + H$	6.020×10^{13}	0.0	0
(28)	$CH_2O + O \Leftrightarrow HCO + OH$	1.820×10^{13}	0.0	3080
(29)	$CH_2O + H \Leftrightarrow HCO + H_2$	3.310×10^{14}	0.0	10 511
(30)	$CH_2O + OH \Leftrightarrow HCO + H_2O$	7.580×10^{12}	0.0	143
(31)	$HCO + O_2 \Leftrightarrow CO + HO_2$	3.000×10^{12}	0.0	0
(32)	$HCO + H \Leftrightarrow CO + H_2$	4.000×10^{13}	0.0	0
(33)	$HCO + OH \Leftrightarrow CO + H_2O$	5.000×10^{12}	0.0	0
(34)	$HCO + O \Leftrightarrow CO + OH$	1.000×10^{13}	0.0	0
(35)	$CH_2O + CH_3 \Leftrightarrow HCO + CH_4$	2.230×10^{13}	0.0	5146
(36)	$CH_3 + OH \Leftrightarrow CH_2O + H_2$	3.980×10^{12}	0.0	0
(37)	$CH_3 + HO_2 \Leftrightarrow CH_4 + O_2$	1.020×10^{12}	0.0	397
(38)	$HO_2 + CO \Leftrightarrow CO_2 + OH$	1.500×10^{14}	0.0	23 645

*Units of B involve gmol cm^{-3} and s.
[1]Non-unity third body coefficients for these reactions are 0.44 for N_2, 0.35 for O_2, 0.74 for CO, 1.47 for CO_2 and 6.5 for H_2O.
[2]Non-unity third body coefficients for these reactions are 5.0 for H_2O.

References

Abugov, D.I. & Obrezkov, O.I. 1978 Acoustic noise in turbulent flames. *Combust. Explos. Shock Waves* **14** (5), 606–612.

Baum, M., Poinsot, T., Haworth, D. & Darabiha, N. 1994 Direct numerical simulation of H2/O2/N2 flames with complex chemistry in two-dimensional turbulent flows. *J. Fluid Mech.* **281**, 1–32.

Baum, M., Poinsot, T. & Thevenin, D. 1995 Accurate boundary conditions for multicomponent reactive flows. *J. Comput. Phys.* **116** (2), 247–261.

Belliard, A. 1997 Etude expérimentale de l'émission sonore des flammes turbulentes. PhD thesis, Université de Provence-Aix-Marseille I.

Bogey, C., Bailly, C. & Juve, D. 2000 Numerical simulation of sound generated by vortex pairing in a mixing layer. *AIAA J.* **38** (12), 2210–2218.

Brouzet, D. 2019 Investigation of direct combustion noise in turbulent premixed jet flames using direct numerical simulations. PhD thesis, University of Melbourne.

Brouzet, D., Dou, X., Talei, M., Gordon, R.L. & Brear, M.J. 2018 Sound generation by planar, CH4/air flame annihilation with several chemical mechanisms. In *Proceedings of the 21st Australasian Fluid Mechanics Conference* (ed. T.C.W. Lau & R.M. Kelso) Australasian Fluid Mechanics Society.

Brouzet, D., Haghiri, A., Talei, M. & Brear, M.J. 2019 Annihilation events topology and their generated sound in turbulent premixed flames. *Combust. Flame* **204**, 268–277.

BURNLEY, V.S. & CULICK, F.E.C. 2000 Influence of random excitations on acoustic instabilities in combustion chambers. *AIAA J.* **38** (8), 1403–1410.

CANDEL, S. 2002 Combustion dynamics and control: progress and challenges. *Proc. Combust. Inst.* **29** (1), 1–28.

CANDEL, S., DUROX, D., DUCRUIX, S., BIRBAUD, A.L., NOIRAY, N. & SCHULLER, T. 2009 Flame dynamics and combustion noise: progress and challenges. *Intl J. Aeroacoust.* **8** (1), 1–56.

CANDEL, S. & POINSOT, T. 1990 Flame stretch and the balance equation for the flame area. *Combust. Sci. Technol.* **70** (1–3), 1–15.

CHAKRABORTY, N. & SWAMINATHAN, N. 2007 Influence of the Damköhler number on turbulence-scalar interaction in premixed flames. I. Physical insight. *Phys. Fluids* **19** (4), 045103.

CHENEAU, B., VIE, A. & DUCRUIX, S. 2015 Large Eddy Simulation of a liquid fuel swirl burner: flame characterization for pilot and multipoint injection strategies. In *Proceedings of the ASME Turbo Expo 2015: Turbine Technical Conference and Exposition*. ASME.

CHENG, R.K. 1984 Conditional sampling of turbulence intensities and Reynolds stress in premixed turbulent flames. *Combust. Sci. Technol.* **41** (3–4), 109–142.

CHIU, H. & SUMMERFIELD, M. 1974 Theory of combustion noise. *Acta Astronaut.* **1** (7–8), 967–984.

CHOI, H. & MOIN, P. 1990 On the space-time characteristics of wall-pressure fluctuations. *Phys. Fluids* A **2** (8), 1450–1460.

CLAVIN, P. 1985 Dynamic behavior of premixed flame fronts in laminar and turbulent flows. *Prog. Energy Combust. Sci.* **11** (1), 1–59.

CLAVIN, P. & SIGGIA, E.D. 1991 Turbulent premixed flames and sound generation. *Combust. Sci. Technol.* **78** (1–3), 147–155.

COFFEE, T.P. 1984 Kinetic mechanisms for premixed, laminar, steady state methane/air flames. *Combust. Flame* **55** (2), 161–170.

COLONIUS, T., LELE, S.K. & MOIN, P. 1997 Sound generation in a mixing layer. *J. Fluid Mech.* **330**, 375–409.

CORREA, S.M. 1998 Power generation and aeropropulsion gas turbines: from combustion science to combustion technology. *Symp. Combust.* **27** (2), 1793–1807.

CUENOT, B., RIBER, E. & FRANZELLI, B. 2014 Towards the prediction of soot in aero-engine combustors with large eddy simulation. In *Proceedings of the Summer Program*, pp. 117–126. Center for Turbulence Research, NASA Ames/Stanford University.

DAVE, H.L. & CHAUDHURI, S. 2020 Evolution of local flame displacement speeds in turbulence. *J. Fluid Mech.* **884**, A46.

DOWLING, A.P. 1992 Thermoacoustic sources and instabilities. In *Modern Methods in Analytical Acoustics*, vol. 92, pp. 378–405. Springer-Verlag.

DOWLING, A.P. & MAHMOUDI, Y. 2015 Combustion noise. *Proc. Combust. Inst.* **35** (1), 65–100.

DUFRESNES, Y., MOUREAU, V., MASI, E., SIMONIN, O. & HORWITZ, J. 2016 Simulation of a reactive fluidized bed reactor using CFD/DEM simulation. In *Proceedings of the Summer Program*, pp. 35–44. Center for Turbulence Research, NASA Ames/Stanford University.

FRANZELLI, B. 2011 Impact of the chemical description on direct numerical simulations and large eddy simulations of turbulent combustion in industrial aero-engines. PhD thesis, Institut National Polytechnique de Toulouse.

FRANZELLI, B., RIBER, E., GICQUEL, L. & POINSOT, T. 2012 Large eddy simulation of combustion instabilities in a lean partially premixed swirled flame. *Combust. Flame* **159** (2), 621–637.

FREUND, J.B. 1997 Proposed inflow/ouflow boundary conditions for direct computation of aerodynamic sound. *AIAA J.* **35** (4), 740–742.

FURUKAWA, J., NOGUCHI, Y., HIRANO, T. & WILLIAMS, F.A. 2002 Anisotropic enhancement of turbulence in large-scale, low-intensity turbulent premixed propane-air flames. *J. Fluid Mech.* **462**, 209–243.

GHANI, A. & POINSOT, T. 2017 Flame quenching at walls: a source of sound generation. *Flow Turbul. Combust.* **99** (1), 173–184.

HAGHIRI, A., TALEI, M., BREAR, M.J. & HAWKES, E.R. 2018 Sound generation by turbulent premixed flames. *J. Fluid Mech.* **843**, 29–52.

HAWORTH, D., BLINT, R.J., CUENOT, B. & POINSOT, T. 2000 Numerical simulation of turbulent propane-air combustion with nonhomogeneous reactants. *Combust. Flame* **121** (3), 395–417.

HILBERT, R., TAP, F., EL-RABII, H. & THÉVENIN, D. 2004 Impact of detailed chemistry and transport models on turbulent combustion simulations. *Prog. Energy Combust. Sci.* **30** (1), 61–117.

HILKA, M., VEYNANTE, D., BAUM, M. & POINSOT, T. 1995 Simulation of flame vortex interactions using detailed and reduced chemical kinetics. In *10th Symposium on Turbulent Shear Flows*, pp. 19–24.

HURLE, I.R., PRICE, R.B., SUGDEN, T.M. & THOMAS, A. 1968 Sound emission from open turbulent premixed flames. *Proc. R. Soc. Lond.* A **303** (1475), 409–427.

HUSSEIN, H.J., CAPP, S.P. & GEORGE, W.K. 1994 Velocity measurements in a high-Reynolds-number. Momentum conserving, axisymmetric, turbulent jet. *J. Fluid Mech.* **258**, 31–75.

IHME, M. 2017 Combustion and engine-core noise. *Annu. Rev. Fluid Mech.* **49**, 227–310.

IHME, M. & PITSCH, H. 2012 On the generation of direct combustion noise in turbulent non-premixed flames. *Intl J. Aeroacoust.* **11** (1), 25–78.

IHME, M., PITSCH, H. & BODONY, D.J. 2009 Radiation of noise in turbulent non-premixed flames. *Proc. Combust. Inst.* **32** (1), 1545–1553.

JIANG, B., GORDON, R.L. & TALEI, M. 2019 Head-on quenching of laminar premixed methane flames diluted with hot combustion products. *Proc. Combust. Inst.* **37** (4), 5095–5103.

JIMENEZ, C., CUENOT, B., POINSOT, T. & HAWORTH, D. 2002 Numerical simulation and modeling for lean stratified propane-air flames. *Combust. Flame* **128**, 1–21.

JIMENEZ, C., HAGHIRI, A., BREAR, M.J., TALEI, M. & HAWKES, E.R. 2015 Sound generation by premixed flame annihilation with full and simple chemistry. *Proc. Combust. Inst.* **35** (3), 3317–3325.

JIMENEZ, C. & KURDYUMOV, V.N. 2017 Propagation of symmetric and non-symmetric lean hydrogen-air flames in narrow channels: influence of heat losses. *Proc. Combust. Inst.* **36** (1), 1559–1567.

KEE, R.J., RUPLEY, F.M. & MILLER, J.A. 1989 CHEMKIN-II: A FORTRAN chemical kinetics package for the analysis of gas-phase chemical kinetics. *Tech. Rep.* SAND-89-8009. Sandia National Labs.

KENNEDY, C.A. & CARPENTER, M.H. 1994 Several new numerical methods for compressible shear-layer simulations. *Appl. Numer. Maths* **14** (4), 397–433.

KLIMENKO, A.Y. & CLASS, A.G. 2000 On premixed flames as gasdynamic discontinuities: a simple approach to derive their propagation speed. *Combust. Sci. Technol.* **160** (1), 23–33.

KO, N.W.M. & DAVIES, P.O.A.L. 1971 The near field within the potential cone of subsonic cold jets. *J. Fluid Mech.* **50**, 49–78.

KOTAKE, S. & TAKAMOTO, K. 1987 Combustion noise: effects of the shape and size of burner nozzle. *J. Sound Vib.* **112** (2), 345–354.

LEYKO, M., NICOUD, F. & POINSOT, T. 2009 Comparison of direct and indirect combustion noise mechanisms in a model combustor. *AIAA J.* **47** (11), 2709–2716.

LOURIER, J.M., STÖHR, M., NOLL, B., WERNER, S. & FIOLITAKIS, A. 2017 Scale adaptive simulation of a thermoacoustic instability in a partially premixed lean swirl combustor. *Combust. Flame* **183**, 343–357.

LOVAS, T., AMNEUS, P., MAUSS, F. & MASTORAKOS, E. 2002 Comparison of automatic reduction procedures for ignition chemistry. *Proc. Combust. Inst.* **29** (1), 1387–1393.

MA, M.C., TALEI, M. & SANDBERG, R.D. 2020 Direct numerical simulation of turbulent premixed jet flames: influence of inflow boundary conditions. *Combust. Flame* **213**, 240–254.

MAGRI, L. 2017 On indirect noise in multicomponent nozzle flows. *J. Fluid Mech.* **828**, R2.

MAGRI, L., O'BRIEN, J. & IHME, M. 2016 Compositional inhomogeneities as a source of indirect combustion noise. *J. Fluid Mech.* **799**, R4.

MARKSTEIN, G.H. 1964 *Non-Steady Flame Propagation*, p. 22. Pergamon.

MATALON, M. 1983 On flame stretch. *Combust. Sci. Technol.* **31** (3–4), 169–181.

MATALON, M. & MATKOWSKY, B.J. 1982 Flames as gasdynamic discontinuities. *J. Fluid Mech.* **124**, 239–259.

METCALFE, W.K., BURKE, S.M., AHMED, S.S. & CURRAN, H.J. 2013 A hierarchical and comparative kinetic modeling study of C1–C2 hydrocarbon and oxygenated fuels. *Intl J. Chem. Kinet.* **45** (10), 638–675.

MITCHELL, B.E. 1996 Direct computation of the sound generated by subsonic and supersonic axisymmetric jets. PhD thesis, Stanford University.

MOORE, C.J. 1977 The role of shear-layer instability waves in jet exhaust noise. *J. Fluid Mech.* **80**, 321–367.

PALULLI, R., TALEI, M. & GORDON, R.L. 2019 Unsteady flame–wall interaction: impact on CO emission and wall heat flux. *Combust. Flame* **207**, 406–416.

PASSOT, T. & POUQUET, A. 1987 Numerical simulation of compressible homogeneous flows in the turbulent regime. *J. Fluid Mech.* **181**, 441–466.

PELCE, P. & CLAVIN, P. 1982 Influence of hydrodynamics and diffusion upon the stability limits of laminar premixed flames. *J. Fluid Mech.* **124**, 219–237.

PETERS, N. 1999 The turbulent burning velocity for large-scale and small-scale turbulence. *J. Fluid Mech.* **384**, 107–132.

PETERS, N., TERHOEVEN, P., CHEN, J.H. & ECHEKKI, T. 1998 Statistics of flame displacement speeds from computations of 2-D unsteady methane-air flames. *Symp. Combust.* **27** (1), 833–839.

POINSOT, T. 2017 Prediction and control of combustion instabilities in real engines. *Proc. Combust. Inst.* **36** (1), 1–28.

POINSOT, T. & VEYNANTE, D. 2005 *Theoretical and Numerical Combustion*, 3rd edn. RT Edwards Inc.

PRICE, R.B., HURLE, I.R. & SUGDEN, T.M. 1969 Optical studies of the generation of noise in turbulent flames. *Symp. Combust.* **12** (1), 1093–1102.

RAJARAM, R., GRAY, J. & LIEUWEN, T. 2006 Premixed combustion noise scaling: total power and spectra. In *12th AIAA/CEAS Aeroacoustics Conference (27th AIAA Aeroacoustics Conference)*. p. 2612. American Institute of Aeronautics and Astronautics.

RAJARAM, R. & LIEUWEN, T. 2009 Acoustic radiation from turbulent premixed flames. *J. Fluid Mech.* **637**, 357–385.

RAMOHALLI, K. 1979 Acoustic diagnostics of the non-premixed turbulent jet flame. In *5th Aeroacoustics Conference*, p. 591. American Institute of Aeronautics and Astronautics.

RIVERA, J., GORDON, R.L., BROUZET, D. & TALEI, M. 2019 Exhaust CO emissions of a laminar premixed propane-air flame interacting with cold gas jets. *Combust. Flame* **210**, 374–388.

RUDY, D.H. & STRIKWERDA, J.C. 1980 A nonreflecting outflow boundary condition for subsonic Navier–Stokes calculations. *J. Comput. Phys.* **36** (1), 55–70.

SANKARAN, R., HAWKES, E.R., CHEN, J.H., LU, T. & LAW, C.K. 2007 Structure of a spatially developing turbulent lean methane-air Bunsen flame. *Proc. Combust. Inst.* **31** (1), 1291–1298.

SCHULLER, T., DUROX, D. & CANDEL, S. 2002 Dynamics of and noise radiated by a perturbed impinging premixed jet flame. *Combust. Flame* **128** (1–2), 88–110.

SHEPHERD, I.G., MOSS, J.B. & BRAY, K.N.C. 1982 Turbulent transport in a confined premixed flame. *Symp. Combust.* **19** (1), 423–431.

SMITH, G., *et al.*1999 http://www.me.berkeley.edu/gri_mech/.

STEINBERG, A.M., DRISCOLL, J.F. & CECCIO, S.L. 2008 Measurements of turbulent premixed flame dynamics using cinema stereoscopic PIV. *Exp. Fluids* **44** (6), 985–999.

STRAHLE, W.C. 1971 On combustion generated noise. *J. Fluid Mech.* **49** (2), 399–414.

STRAHLE, W.C. 1978 Combustion noise. *Prog. Energy Combust. Sci.* **4** (3), 157–176.

STRAHLE, W.C. 1985 A more modern theory on combustion noise. In *Recent Advances in the Aerospace Sciences* (ed. C. Casci), pp. 103–114. Springer.

SWAMINATHAN, N., XU, G., DOWLING, A.P. & BALACHANDRAN, R. 2011 Heat release rate correlation and combustion noise in premixed flames. *J. Fluid Mech.* **681**, 80–115.

TALEI, M., BREAR, M.J. & HAWKES, E.R. 2011 Sound generation by laminar premixed flame annihilation. *J. Fluid Mech.* **679**, 194–218.

TAM, C.K., BAKE, F., HULTGREN, L.S. & POINSOT, T. 2019 Aircraft noise generation and assessment. *CEAS Aeronaut. J.* **10** (1), 101–122.

THOMAS, A. & WILLIAMS, G.T. 1966 Flame noise: sound emission from spark-ignited bubbles of combustible gas. *Proc. R. Soc. Lond.* A **294** (1439), 449–466.

THORNBER, B., BILGER, R.W., MASRI, A.R. & HAWKES, E.R. 2011 An algorithm for LES of premixed compressible flows using the conditional moment closure model. *J. Comput. Phys.* **230** (20), 7687–7705.

TRIVEDI, S., GRIFFITHS, R., KOLLA, H., CHEN, J.H. & CANT, R.S. 2019 Topology of pocket formation in turbulent premixed flames. *Proc. Combust. Inst.* **37** (2), 2619–2626.

TRUFFAUT, J. 1998 Étude expérimentale de l'origine du bruit émis par les flammes de chalumeaux. PhD thesis, Université de Provence-Aix-Marseille I.

VREMAN, A.W., VAN OIJEN, J.A., DE GOEY, L.P.H. & BASTIAANS, R.J.M. 2009 Subgrid scale modeling in large-eddy simulation of turbulent combustion using premixed flamelet chemistry. *Flow Turbul. Combust.* **82** (4), 511–535.

WANG, H., HAWKES, E.R. & CHEN, J.H. 2016 Turbulence-flame interactions in DNS of a laboratory high Karlovitz premixed turbulent jet flame. *Phys. Fluids* **28** (9), 095107.

WELCH, P. 1967 The use of fast Fourier transform for the estimation of power spectra: a method based on time averaging over short, modified periodograms. *IEEE Trans. Audio Electroacoust.* **15** (2), 70–73.

WILFERT, G., SIEBER, J., ROLT, A., BAKER, N., TOUYERAS, A. & COLANTUONI, S. 2007 New environmental friendly aero engine core concepts. In *18th International Symposium on Air Breathing Engines, AIAA Paper 2007–1120*.

WILLS, J.A.B. 1964 On convection velocities in turbulent shear flows. *J. Fluid Mech.* **20** (3), 417–432.

WU, X. & MOIN, P. 2008 A direct numerical simulation study on the mean velocity characteristics in turbulent pipe flow. *J. Fluid Mech.* **608**, 81–112.

ZHANG, F., HABISREUTHER, P., BOCKHORN, H., NAWROTH, H. & PASCHEREIT, C.O. 2013 On prediction of combustion generated noise with the turbulent heat release rate. *Acta Acust. United Acust.* **99** (6), 940–951.

ZHANG, S. & RUTLAND, C.J. 1995 Premixed flame effects on turbulence and pressure-related terms. *Combust. Flame* **102** (4), 447–461.

ZHANG, Z., ZHAO, D., LI, S.H., JI, C.Z., LI, X.Y. & LI, J.W. 2015 Transient energy growth of acoustic disturbances in triggering self-sustained thermoacoustic oscillations. *Energy* **82**, 370–381.

ZHENG, X.L., LU, T. & LAW, C.K. 2007 Experimental counterflow ignition temperatures and reaction mechanisms of 1,3-butadiene. *Proc. Combust. Inst.* **31** (1), 367–375.

ZHOU, J., ADRIAN, R.J., BALACHANDAR, S. & KENDALL, T.M. 1999 Mechanisms for generating coherent packets of hairpin vortices in channel flow. *J. Fluid Mech.* **387**, 353–396.